UNIVERSIDAD NACIONAL AUTÓNOMA DE MÉXICO
PROGRAMA DE MAESTRÍA Y DOCTORADO EN INGENIERÍA
ENERGÍA

ESTUDIO DE VORTICES HELICOIDALES EN LA ESTELA DE UN AEROGENERADOR

T E S I S

QUE PARA OPTAR POR EL GRADO DE:
MAESTRO EN INGENIERÍA

PRESENTA:
OLIVER DE LA CRUZ PIÑA RUIZ

TUTOR PRINCIPAL:
DR. EDUARDO RAMOS MORA
INSTITUTO DE ENERGÍAS RENOVABLES, UNAM

MÉXICO, D. F. JULIO 2014

JURADO ASIGNADO

Presidente:	Dr. Cuevas García Sergio
Secretario:	Dr. Ramos Mora Eduardo
Vocal:	Dr. Avila Rodríguez Rubén
1er. Suplente:	Dr. Campos Amezcua Rafael
2do. Suplente:	Dr. Jaramillo Salgado Oscar Alfredo

Lugar donde se realizó la tesis:

INSTITUTO DE ENERGÍAS RENOVABLES

TUTOR DE TESIS:

Dr. Eduardo Ramos Mora

FIRMA

AGRADECIMIENTOS

Al conjunto de trabajadores que laboran en el Instituto de Energías Renovables por las facilidades otorgados a lo largo de los estudios.

Al Consejo Nacional de Ciencia y Tecnología (CONACyT), por brindarme su apoyo económico.

A la Universidad Nacional Autónoma de México y en especial al Instituto de Energías Renovables por permitirme realizar mis estudios de maestría en sus instalaciones.

Al Dr. Eduardo Ramos Mora, por su asesoría.

Contents

Abstract

In this work the study of the wake of a wind turbine was done through the inclusion of helical vortices in it. The helical geometry was chosen because several experimental studies have shown that turbines, propellers and helicopter rotors generate such vortices, in which the vorticity is confined. The study of these helical vortices was performed by numerical simulations which were validated with the model of Hardin. Validation was done for two different advances, one where the filament is compressed ($2\pi k = 1$) and the other where this is expanded ($2\pi k = 6$). Hardin's model is the analytical solution of the velocity field generated by a single helical filament. In the study of the analytical solution was observed that this presents a lack of convergence in the velocity components for some values of the azimuthal coordinate (ϕ). Mainly when the series of the Hardin's model are evaluated close to the radius of the filament. The comparison between analytical and numerical model showed to have a good qualitative agreement mainly in the radial and azimuthal component of the velocity. But the axial component had more diffences, especially when the advance was equal to one. From the numerical model was done the study of the velocity field generated by three filaments, this was done with the idea of simulating conventional turbines with three blades, and the results have agreement with that reported in the literature. Due to the observed diffences between the analytical and numerical model, it was done a study of convergence of the models, which was based on the axial component. This study shows that the numerical model does not behave as the analytical model for this velocity component, when the advance is equal or lower than one. This was attributed to that analytical model is based on an infinite helical vortex, while the numerical is based on finite one. The aerodynamic study of a wind turbine was done through of the Tavares's model, which takes into account the effects in the wake by including a Rankine vortex. In this study, it was observed that the analysis performed has good agreement with that reported by Tavares, but it was also observed some discrepancies especially in the chord, which was attributed to the calculation of the tip loss factor. The coupling of the helical wake with the blade element theory (BEM) was done through the Tavares's model. The results show that the circulation of the helical vortices have a strong influence in the convergence of the BEM, which matches with that reported in the literature. Further, it was also observed that this coupling has good results especially for high tip speed ratios.

Chapter 1

Introduction

1.1 Wind energy

A renewable resource is a source that can provide energy in an almost unlimited way. Renewable energy produced using fuel sources that are practically inexhaustible in human scales, or are quickly renewed through natural processes, like solar energy, wind energy, hydropower, geothermal, biomass, ocean energy and tidal power[1]. It is a remarkable fact that in contrast to the case of nonrenewables, the renewablenenergies will tend to become less expensive as the scale of their use increase[2]. Initially, the renewables can be more expensive because the price we pay for conventional power does not reflect the full cost of their environmental impacts, at the same time the renewable energy provides benefits that are not priced, such as: helping to keep our air clean; making use of secure, indigenous, and replenishable natural resources; potential to reduce the production of carbon dioxide among others[1].
Wind energy has been harnessed since a long time by the man, mainly for sailing and milling. Since that distant when our ancient ancestor first learned to rig sails on their rafts, wind power has been used. After this early discovery, the use of wind progressed rapidly to the point that all the world's navies and transoceanic commerce were powered by it, the large sailing vessels of the 19^{th} century could extract as much as $10,000$ horsepower from the wind[2]. According to historians, the first machines utilizing wind energy were used in the orient, as early as 1700 BC, Hammurabi is supposed to have employed windmills to water the planes of Mesopotamia, there is written evidence of the quite early utilization of wind power in Afghanistan. Otherwise, it is knows that the earth's winds are a direct consequence of solar energy, on both local and global scales, these winds are generated because the sun heats certain areas of the earth's surface and atmosphere more than others, the differential heating induces both vertical and horizontal air currents which are modified by the earth's rotation and contours of the land[2]. About 2% of solar incident radiation is transformed into kinetic energy of the wind, and this energy is dissipated into warming the atmosphere and gainst features of the aerth's surface as fast as is gained from the solar heating, thus maintaining at a quite steady average amount[2]. For example, the amount of solar radiation absorbed at the earth's surface is greater at the equator than at poles, and so the variation in incoming energy sets up convective cells in the lower layers of the atmosphere, thus the air rises at the equator and sinks at the poles[3]. The land-sea breeze cycle is an example of how the wind is produced, during the daytime the sun shines on both land and sea, but the surface of the land becomes significantly

warmer than surface of the sea because it takes less energy, as the air over the warm land is heated, it rises and is replaced by the onshore breeze that moves air in from over cooler sea, after the sun sets the land and the air over it cools faster than the sea, then the now warmer air over the sea rises and is replaced by an offshore breeze that moves the heavier cooler air out from over land[2]. Another parameter that plays an important role in the movement of wind is the circulation of the atmosphere, which it results from uneven heating, in addition of the seasonal variations in the distribution of solar radiation and the effects of the rotation of the earth, at a speed of about 600 kilometers per hour at the equator and decreasing to zero at the poles. The spatial variations in heat transfer to the earth's atmosphere create variations in the atmospheric pressure field that cause air to move from high to low pressure, the pressure gradient force in the vertical direction is usually canceled by the downward gravitational force, moreover the atmospheric winds are also influenced by the inertia of the air, the earth's rotation, and friction with the earth's surface [3]. Numerous studies and date from the turbines have helped to make estimates of the wind power or energy potential of regions of the earth and of the entire earth itself, usisng these estimates we can assess the electrical power producing potential of wind energy in that region, the wind resource estimation consists of the determination of the productivity of a given wind turbine at a given site where wind speed information is available in either time series format or in a summary format [3]. The World Energy Council determined in 1993, the following five categories of wind resource:

- Meteorogical potential, this is equivalent to the available wind resource.
- Site potential, this is based on the meteorological potential, but is restricted to those sites that are geographically available for power production.
- Technical potential, is calculated from the site potential accounting for the available technology
- Economic potential, is the technical potential that can be realized economically.
- Implementation potential, takes into account constraints and incentives to assess the wind turbine capacity that can be implemented within a certain time frame.

An important parameter in the characterization of the wind resource is the variation of horizontal wind speed, we would expect the horizontal wind speed to be zero at the earth's surface and to increase with the height, this varation of wind speed is called the vertical profile of the wind speed or vertical wind shear. In engineering the determination of the vertical wind shear, is an important parameter of design because determines directly the productivity of a wind turbine and it can strongly inflence the lifetime of a turbine rotor blade, the fatigue life of a rotor blade is influenced by the cyclic loads resulting from rotating through a wind field that varies in the vertical direction, there are two basics problems in the determination of vertical wind profile for wind energy aplications and are: instantaneous variation of wind speeds as a function of height,seasonal variation of average wind speeds as a function of height. To determine the wind energy resource in a

site, is necessary to collect a large date of data for a period of time, this data could include direction data, as well as wind speed data, and with them we could evaluate the wind resource or wind power production potential,this analysis can be accomplished through of direct or statistical techniques[3].
The wind power available is the energy in the wind that it can be converted into a useful form of energy, and its estimation is derived of the fluid mechanics, from the continuity equation(1.1),

$$\frac{dm}{dt} = \rho A U \tag{1.1}$$

where dm/dt is the mass flow of air through a rotor disk, A area, ρ is the density, and U is the air velocity, in addition the knetic energy per unit time, or power, of the flow is given by:

$$P = \frac{1}{2}\frac{dm}{dt}U^2 = \frac{1}{2}\rho A U^3 \tag{1.2}$$

the wind power per unit area, P/A or wind power density is:

$$\frac{P}{A} = \frac{1}{2}\rho U^3 \tag{1.3}$$

The wind power increases rapidly with velocity and it is proportional to the third power of the velocity, namely each unit of air mass has kinetic energy proportional to the square of its velocity, and the amount of air mass moving past a given point (for instance, the location of a windmill) per unit of time is proportional to the wind velocity, thus the amount of power (energy/time) varies as v^3 at any point in the space[2]. The actual power production potential of a wind turbine must take into account the fluid mechanics of the flow passing through rotor, and the aerodynamics and efficiency of the rotor/generator. In practice cannot be extracted completely the wind power for a turbine, because this means that the air flow had to stop completely within the intercepting rotor area, which would congest the cross sectional area for the following air[4]. Although the wind energy is considered a clean energy, it has environmental impact mainly on land, noise, effects on wildlife and disruption of radio transmissions, however, this impact it is not so considerable, because the lands used for wind farms also can be used for grazing of animals, as well as in the case of noise it has proposed that wind turbines are located at least a distance of $300m$ from the human because at this distance the decibel of the turbine are similar to the decibel in a library, besides that several environmental groups have voiced their concern about the negative effect on bird populations due wind farms, recent studies of the “Royal Society For The Protection For Birds” have shown wind turbines to have very little effect on bird populations, the damage to wildlife habitat caused by traditional fossil has a much greater impact on wildlife than wind energy. Other benefits of using wind energy are: it avoids most of the traditional enviromental impacts associated with electricity generation, does not result in the risks or radiative exposure associated with nuclear power plants, helps to reduce the problems of global warming and acid rain[1].

Furthermore, noise and visual impact will be less significant in the future as more wind turbines will be sited offshore[5].

1.2 Wind turbines

A wind turbine transforms the kinetic energy in the wind to mechanical energy in a shaft and finally into electrical energy in a generator, in practice one cannot reduce the wind speed to zero, so a power coefficient C_P is defined as the ratio between the actual power obtained and the maximum available power,theoretically exist a maximum C_P denoted as the Betz limit $C_{Pmax} = 16/27 = 0.593$, the modern turbines operate close to this limit with a C_P up to 0.5[5]. Otherwise, the windmills can be considered as ancestor of the modern wind turbines, as already mentioned these served mainly to mill grain or pump water, the world's oldest windmills had a vertical axis, braided mats were attached to the axis, the mats caused drag forces and, therefore, were carried along by the wind[4]. Subsequently it was discovered, that it was more efficient to use the lift forces than drag forces to extract energy and later models moved to this type of operation, lift and drag are the components of the force perpendicular and parallel to the direction of the relative wind respectively[5]. Windmills were widely used in the Islamic world and it was not until the Middle Ages when they were introduced to Europe by returning crusaders, they had a great development mainly in three countries, denmark, germany and holland, but holland introduced many improvements in the design and, in particular the rotors, by the sixteenth century, the primitive jib sails on wooden booms had given way to sails supported by wooden bars on both sides of the stock, and later the bars were moved to the trailing edge of the rotor to improve the aerodynamics design[6].

- Horizontal axis rotors, for which the axis of rotation is parallel to the direction of the windstream.
- Vertical axis rotors, for which the axis of rotation is perpendicular to both surface of the earth and the windstream.
- Crosswind horizontal rotors, for which the axis of rotation is both horizontal to the surface of the earth and perpendicualr to the direction of the windstream.

The horizontal axis rotors are also known as horizontal axis wind turbines (HAWT), they are most commonly used because for a given area, high rotational speeds and more output power can be developed by the lift than by drag forces, a lift device can move faster than the wind velocity, while a drag device cannot[6]. A HAWT is described in terms of the rotor diameter, the number of blades, the tower height, the rated power and the control strategy, the tower is important since wind speed increases with heigh above of ground, and the rotor diameter is important since this gives the area to calculate the power available. In these devices usually is common to use two or three blades, but the aerodynamic efficiency is lower on a two-bladed than a three-bladed wind turbine (see

Fig. 1.1), usually the two-bladed is known as downstream turbine, and the three-bladed as upstream turbines. Furthermore, the connection of the shaft to the rotor is more flexible in a two-bladed, this produces no bending moments are transferred from the rotor to the mecahnical shaft, but they are noiser and more unstable than upstream turbines. The rotational speed of a wind turbine rotor is apporoximately 20 to 50 rpm and the rotational speed of most generator shafts is approximately 1000 to 3000 rpm, therefore in these systems is necessary a gearbox, which it must do the transmission between low-speed rotor shaft and the high-speed generator shaft. Ideally a wind turbine rotor should always be perpendicular to the wind, therefore is mounted on the turbine a wind vane to mesure the direction of the wind, this signal is coupled with a yaw rotor, which continuously turns the nacelle into the wind[5].

Figure 1.1: HAWT of three blades

The vertical axis rotors are also known as horizontal axis wind turbines (VAWT), in general they have a major advantage over HAWT, which it is that they do not turned into the wind, this reduces the design complexity of the system and decreases gyro forces on the rotors. Many types of VAWT has been developed, which they use the drag force to turn the rotors, these include those panemones that use plates, cups, as well as the Savonius S-shaped cross-section which actually provide some lift force, such devices have relatively high starting torques compared to lift devices, but have lower output power per given rotor size, weight and cost. The Darrieus rotor (see Fig. 1.2) was invented by Darrieus G., in 1920 and it is considered the VAWT with major potential, it is a lift device characterized by curved blades with airfoil cross sections, generally it has low solidity and low starting torques, but high tip-to-wind speeds and therefore relatively high output power. Several types of Darrieus has been developed, which they can be designed to operate with one, two, three, or more blades, depending on the application of

the turbine. Several Crosswind horizontal devices have been developed, but they are not very used, mainly to their low output power, which is due to these devices must be turned into the wind and as the wind direction changes, they do not appear to have significant advantages over HAWT and VAWT[6].

Figure 1.2: Darrieus rotor of two blades

1.3 Why is it important the study of helical vortices?

The helical vortices occurs naturally in many practical problems in aerodynamics, geophysics and engineering sciences. For example, they are observed in tip vortices behind wings and propellers, in atmospheric tornadoes and cyclones, and in flame holders in combustion devices[7]. In addition the experimental results indicate that such distributions are a prominent instability mode in high subsonic circular free jet flows, thus the study of helical vortices is of considerable physical interest[8]. Otherwise, experimental observations in a rotating lid-driven cavity have revealed that the phenomenon of vortex breakdown is related to the creation of helical vortices, the results were in excellent agreement with stability analysis. Vortex breakdown is characterized by a structural change of the vortex core, associated with an abrupt decelaration of the axial velocity on the vortex axis, which sometimes develops into a recirculation zone. Although there are seven

different states of breakdown, bubble and the spiral are the two predominant breakdown configurations, and only the double helix contains stable multiple modes[7]. Indeed, a stable couple of helical vortices has been observed many times in various vortex flows, triplets of helical vortices in the flows is a far less frequent case, while configuration of four vortex structures is an even more unstable phenomenon[9]. Otherwise, the flow behind rotor systems, such as helicopters, wind turbines and propellers, consists of a vortex sheet which is formed by the lift distribution along the blades. Due to the interaction between the vortex elements a roll-up process sets in immediately after the vortex sheet is created, which forms strong tip and root vortices in the immediate near-wake behind the rotor. In most cases, the tip/root vortex system is unstable, and due to various instability mechanisms it eventually breaks down and forms small-scale turbulence further downstream[10, 11]. The wake can generally be divided into two distinct parts, near wake and far wake. Near-wake features are related to the genesis of the vortex system where the presence of the rotor is felt directly through the formation of the vortex system. The far wake is usually the downstream position where the wake dynamics no longer depends on specific rotor characteristics and where the flow has broken down and is dominated by small-scale turbulence[10, 11]. Modern wind turbines are often grouped in large parks where the turbines located in the interior of the park are exposed to wake flows from the surrounding turbines. This increases the fatigue loads and hence reduces the lifetime of the turbines. In most cases, the vortices become unstable and break down. It is obvious that if a wind turbine is located in a wake consisting of stable tip vortices, the fatigue loading is more severe than if the vortices have broken down by instability[10, 11, 12].

1.3.1 Helical vortices

The first examination of a helical vortex filament was carried out by Levy and Forsdyke, they found that a filament is stable in that it will maintain its shape under its own induced velocity field, also they determinated that it will convect in the direction of its axis with steady speed and rotate about that axis with uniform angular velocity[13]. Otherwise, Widnall in 1972 realized a stability study of a helical vortex filament of finite core and infinite extent to small sinusoidal displacements of its centre line. The influence of the entire perturbed filament on the self-induced motion of each element is taken into account. The effect of the details of the vorticity distribution within the finite vortex core on the self-induced motion due to the bending of its axis is calculated. The results of the stability calculations presented in this paper show that the helical vortex filament has three modes of instability: a very short wave instability which probably exists on all curved filaments; a long wave mode which is also found to be unstable by the local induction model and a mutal inductance mode which appears as the pitch of the helix decreases and the heighbouring turns of the filament[14]. Betchov like Widnall was one of the first to study the stability of helical vortex to small sinusoidal displacements of its centre line. Betchov considered that each portion of the filament moves with a velocity that can be approximated in terms of the local curvature of the filament. He found that helical vortex filaments are elementary solutions, and that they are unstable, in addition

he was only able to find one stability mode[15]. Moreover, adebiyi studied the existence of helical vortex tubes of small cross section in an inviscid fluid by introducing a stream function for the flow, in this study the expressions were obtained for the propagation speed , circulacion, and cross-sectional area of the helical vortex tubes[16]. An analytical solution for the velocity field induced, both interior and exterior by an infinite right-handed helical vortex filament was developed by Hardin. The solution is obtained as infinite series, essentially of the Kapteyn type, which converge rapidly enough. Also it is shown that it is possible to derive a stream function for this nonaxisymetric flow, due to the combination of variables in the solution. The expressions obtained are of great interest because they can be used to validate numerical integration techniques for the Biot-Savart law, as well as for modelling wakes of propeller and rotors[8]. The classical problem of linear stability of a regular N-gon of point vortices to infinitesimal space displacements from an equilibrium of the vortex configuration was generalized to the one for N helical vortices by Okulov, he obtained the analytical form for the stability boundaries, this solution allows an efficient analysis to be made of the existence of stable helical vortex arrays whitin the whole range of helical pitch variations[9]. Later, Okulov and Fukumoto developed a solution of the velocity field induced by a helical vortex tube, in which they take into account the influence of finite-core thickness on the velocity field, and they developed an asymptotic expansion of the Biot-Savart law to a higher order in small parameter, in addition the velocity field was determinated due to influence of dipoles. They obtained the velocity field in form of the Kapteyn series, which is in agreement with Hardin's solution for monopoles[8]. They found that the velocity field is small near of the axis of the supporting cylinder, but becomes larger as the cylinder is approached. For vortex rings, the accuracy of the asymptotic expansion of the Biot-Savart law near the core is better than expected, since the magnitude of the coefficients decreases exponentially with the order of the expansions[17].

1.4 Study of the vorticity in the wake

Several studies have been conducted in the wake of rotors or propellers, in which it has taken into account the vorticity, either for the calculation of instabilities or for a better understanding the behavior of the turbines or propellers. Below we mention some of these studies we have found in the literature.
Gupta and Loewy were the first to consider tip vortices in rotor far wakes, their analysis dealt with the stability of centreline perturbations of the helical vortex system. They found that the helical vortices were unstable, however this result is in contradiction to visualizations of rotor wakes showing that helical tip vortices subject small pitch values are stable[18]. Later, an analysis of stability in helicopter rotor wakes was developed by Leishman, it shown that the rotor wake is intrinsically unstable, with the tip vortices exhibiting several possible unstable deformation modes, the wake divergence rate is associated with each deformation mode depends on the relative phase of the perturbations produced on tip vortex filaments[19]. Otherwise, Sørensen and Shen developed a numerical model for predicting global flow fields of wind turbines, this model was based on a so-called actuator

line concept in which the blade loading was introduced in the Navier-Stokes equations as body forces. The model had a good agreement with experimental results, in addition it demonstrated that the global flow field about the rotor is well represented by letting the loading on the blades be determinated by body forces distributed along lines. Also, the axial interference factor in the rotor plane and the position of the tip vortices in the near wake were analyzed in detail[20]. Moreover, Okulov in 2004 studied the problem of stability of the equilibrium circular configuration behind propellers and wind turbines where the vorticity is concentrated in N helical tip vortices and hub vortices. The theoretical model shown that these systems are unstable which it is at variance with the numerous visualizations of wind-turbine and propeller wakes too where the helical tip vortices with small pitch usually exist with negligible changing in a long trail behind the turbine[9]. Thereafter, Okulov and sørensen carried out the analysis of stability behind wind turbine, they used an $(N + 1)$-vortex system like model for the wake, which it moves in uniform airflow at a constant wind speed V, and since the flow behind the wind turbine has a wake like profile, they employed a system of left-handed helical vortices. They found that, even with a rough estimate of the system vortex parameters in terms of turbine operating characteristics, the theory developed is qualitatively consistent with data from full-scale and model tests, and that the representation of the correlation equation in the simple analytical form can be considered a first step in finding recommendations for efficient control of wind-turbine clustered in parks, or wind farms[12]. Subsequently they developed, a second stability analysis of the wake behind a multi-bladed rotor, where the wake was modeled with tip vortices, which they were approximated as infinitely long helical vortices with constant pitch and radius. This work includes an assigned vorticity field due to root vortices and the hub of the rotor, thus the tip vortices are assumed to be embedded in an axisymmetric helical vortex field formed from the circulation of the inner part of the rotor blades and the hub. The results show that the stability of the tip vortices largely depends on the radial extent of the hub vorticity as well as on the type of vorticity distribution. Comparison with experiments shows that the considered vortex model gives an excellent representation of the far wake behind a wind turbine[11]. Finally, they developed a new model for a rotor with a finite number of blades and constant circulation. The method was based on an analytical solution to the problem of equilibrium motion of a helical vortex multiplet in a far wake. The vortex system behind the rotor is represented by a set of helical vortices with finite core to eliminate the singularity of the induced velocity field in the vicinity of each filament. The main achievement of the model was that it eliminated the singularity of the solution at all operating conditions. In contrast to earlier models, the new model enables for the first time to determine the theoretical maximum efficiency of rotors with constant circulation and an arbitrary number of blades[21]. We can note that Okulov and Sørensen are some of the researchers who have been more concerned about a better understanding of the behavior of the wakes of wind turbines. As well as, the study of the vortex system behind a wind turbine and instability problem that results in the generation of such vortices. Otherwise, Ivanell and et al. did a numerical study about rotor wakes based in model developed by Sørensen and Shen[20], in this study they imposed disturbances upstream of a three bladed rotor to determine the receptivity to various frequencies. They shown that the instability is dispersive and that growth arises

for specific frequencies and modes with wavenumbers equal to half integer multiples of the number of blades. Furthermore, they observed that the mutual inductance instability is associated with vortex pairing[22]. In 2011 Felli and et al. developed a experimental study of a marine propeller, they used comprehensive velocity measurements and high speed flow visualizations for that, besides different advance ratios and number of blades. They were able to observe the onset of instabilities in a system of helical vortices, in addition the strength of the tip vortex was estimated using an additional inviscid numerical simulation. From this, it seems that the circulation of the hub vortex depends on the number of blades and advance ratio, whereas the strength of the tip vortices, remains the same regardless of the different propeller configurations. Another important observation was that the amplification rate of the mutual inductance-instability mode increases with increased propeller loading, partly because of a reduction in wake pitch and partly because of the creation of larger core sizes[23].
The Fig. 1.3 shows an experimental study about of trailing vortices generated by a wind turbine, in this visualization the smoke is inserted into the flow from an external nozzle, the picture shows the cross section of the tip vortices, where the vorticity is confined. Otherwise, the Fig. 1.4 shows another experimental study of the vorticity in a wind turbine, in thi experiment the smoke was emanated from the tip of the model, the smoke trail revealed the path of the tip vortex as a helical[24].

Figure 1.3: Flow visualization of the trailing vortices behind a wind turbine[24]

From the discussion above, we can observe that various efforts have been realized to understand the vortex systems behind of wind turbines or propellers. These efforts have been developed in several areas such as analytical, experimental and numerical, where the results have shown good agreement for some cases given. Nevertheless, there is controversy in several studies due to lack of agreement between the numerical and experimental results, and the same occurs when we compare an analytical model with an experiment. This fact proves that the behavior of the flow behind a turbine or propeller is difficult to model

Figure 1.4: Flow visualization with smoke generated in tip, revealing smoke trails for the NREL turbine in the NASA-Ames[24]

both analytically or numerically. In addition, often the flow is complex which it makes more difficult the analysis.

Chapter 2

Mathematical description of helical vortices

In many cases of study, the fluid containing vorticity occupies only a small fraction of the total fluid volume, and for incompressible flows it is sufficient to follow only the evolution of the vorticity field. The velocity field can be determinated from the vorticity field and boundary conditions. Moreover from the theorems of Helmholtz and Kelvin, we know that for a uniform-density inviscid fluid,the tubes of vorticity retain their identity and move as material entities [25]. Based on these assumptions and the experimental observations, it can be proposed the study of the wake of a wind turbine using helical vortices. The analitical model was developed to study the velocity field generated by a single helical infinite filament. This solution is expressed in infinite series that are given in terms of Bessel functions. The numerical method used in this work was developed for aerodynamic studies, mainly with the aim of simulating complex flows with low computational effort. This method is based in the numerical integration of the Biot-Savart law.

2.1 Analytical model

The analitical solution of the velocity field induced by a helical vortex filament was developed by Hardin [8]. He used the expressions given by Lamb [26] for the velocities in the three-coordinate directions induced at the point (x, y, z) by an arbitrary vortex filament in an infinite mass of incompressible fluid. The theory starts by introducing the following integral:

$$I(\alpha) = \int_{-\infty}^{\infty} \frac{e^{(i\alpha\theta)} d\theta}{r}, \tag{2.1}$$

where $r^2 = (x - x')^2 + (y - y')^2 + (z - z')^2$, and $x' = \mathrm{acos}\theta$, $y' = \mathrm{asin}\theta$, $z' = \mathrm{k}\theta$ are the parameters that define the helical curve in a Cartesian coordinate system fixed to the filament, as defined in Fig. 2.1, where a is the radius of the circumscribing cylinder, θ is the polar angle of a position the helix, and $2\pi k$ is its pitch. The position of an arbitrary point in space is given by $x = \rho\mathrm{cos}\phi$, $y = \rho\mathrm{sin}\phi$ and z. The limits of the integral indicate that all points in the helix contribute to the calculation of the velocity (see equations 2.2-2.4).

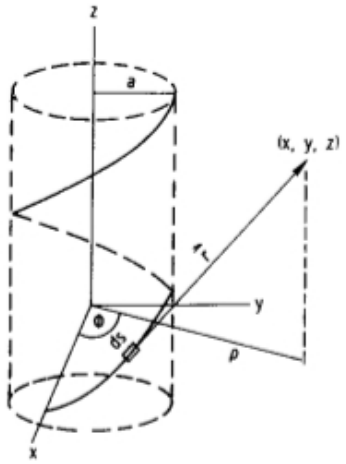

Figure 2.1: Geometry of the helical vortex filament

The Cartesian velocity components induced by an infinite helical vortex are:

$$u = \frac{\Gamma}{4\pi}(k\frac{\partial I_1}{\partial y} - a\frac{\partial I_2}{\partial z}), \tag{2.2}$$

$$v = \frac{-\Gamma}{4\pi}(k\frac{\partial I_1}{\partial x} + a\frac{\partial I_3}{\partial z}), \tag{2.3}$$

and

$$w = \frac{\Gamma a}{4\pi}(\frac{\partial I_2}{\partial x} + \frac{\partial I_3}{\partial y}), \tag{2.4}$$

where Γ is the circulation of the vortex filament,

$$I_1 = I(0), \qquad I_2 = Re[I(1)], \qquad I_3 = Im[I(1)],$$

Re and Im indicate the real and imaginary parts of the complex expressions. The parameter r can be expressed in terms of the coordinates of the position vector as:

$$r^2 = (\rho\cos\phi - a\cos\theta)^2 + (\rho\sin\phi - a\sin\theta)^2 + (z - z')^2, \tag{2.5}$$

expanding and factoring, Eq. (2.5) becomes

$$\begin{aligned} r^2 &= \rho^2(\cos^2\phi + \sin^2\phi) + a^2(\cos^2\theta + \sin^2\theta) \\ &\quad -2a\rho(\cos\phi\cos\theta + \sin\phi\sin\theta) + (z - k\theta)^2. \end{aligned} \tag{2.6}$$

If we now use the law of cosines and take $r_0 = \rho^2 + a^2 - 2\rho a\cos(\phi - \theta)$, we get

$$I(\alpha) = \int_{-\infty}^{\infty} \frac{e^{(i\alpha\theta)}d\theta}{[r_0^2 + (z - k\theta)^2]^{1/2}}, \tag{2.7}$$

In order to integrate Eq. (2.7), we recall the following relation given by Watson[27],

$$\frac{1}{R} = \int_0^{\infty} e^{-|s|\lambda} J_0(r_0\lambda)d\lambda, \tag{2.8}$$

where J_0 is the Bessel function of first kind and zeroth order and

$$\begin{aligned} s &= z - k\theta, \\ R^2 &= r_0^2 + s^2, \end{aligned}$$

The bessel function $J_0(\lambda r_0)$ can be expanded as

$$J_0(\lambda r_0) = \sum_{m=0}^{\infty} \epsilon_m J_m(\lambda\rho)J_m(\lambda a)\cos m(\phi - \theta) \tag{2.9}$$

where,

$$\epsilon_m = \begin{cases} 1 & m{=}0 \\ 2 & m{\neq}0 \end{cases}$$

using expressions (2.8) and (2.9), the function I(α) becomes

$$I(\alpha) = \sum_{m=0}^{\infty} \epsilon_m \int_0^{\infty} d\lambda J_m(\lambda\rho)J_m(\lambda a) \times \int_{-\infty}^{\infty} e^{i\alpha\theta}e^{-|z-k\theta|\lambda}\cos m(\phi - \theta)d\theta, \tag{2.10}$$

the integral with respect to θ is:

$$\int_{-\infty}^{\infty} e^{i\alpha\theta}e^{-|z-k\theta|\lambda} \quad \cos m(\phi - \theta)d\theta = \frac{\lambda e^{i\alpha(z/k)}}{k}\left(\frac{e^{im[\phi - z/k]}}{\lambda^2 + [(m-\alpha)/k]^2} + \frac{e^{-im[\phi - z/k]}}{\lambda^2 + [(m+\alpha)/k]^2}\right). \tag{2.11}$$

Combining Eq. (2.10) and Eq. (2.11), we get:

$$I(\alpha) = \sum_{m=0}^{\infty} \epsilon_m \frac{e^{i\alpha(z/k)}}{k}$$
$$\left[e^{im(\phi - z/k)} \int_0^{\infty} \frac{J_m(\lambda\rho)J_m(\lambda a)\lambda d\lambda}{\lambda^2 + [(m-\alpha)/k]^2} + e^{-im(\phi - z/k)} \int_0^{\infty} \frac{J_m(\lambda\rho)J_m(\lambda a)\lambda d\lambda}{\lambda^2 + [(m+\alpha)/k]^2} \right]. \quad (2.12)$$

Now to evaluate Eq. (2.12) with $\alpha = 0$, we expand on m, and identify two cases: $m = 0$ and $m \neq 0$. For $m = 0$ the first term in the sum is

$$\frac{2}{k} \int_0^{\infty} \frac{J_0(\lambda\rho)J_0(\lambda a)}{\lambda} d\lambda \quad (2.13)$$

For $m \neq 0$ we use the following relation given by watson[27],

$$\int_0^{\infty} \frac{\lambda J_m(\lambda\rho)J_m(\lambda a)}{\lambda^2 + [(m \pm \alpha)/k]^2} d\lambda = I_m \left(\left| \frac{m \pm \alpha}{k} \right| \rho_s \right) K_m \left(\left| \frac{m \pm \alpha}{k} \right| \rho_g \right).$$

Valid for $m \pm \alpha \neq 0$. I_m and K_m are modified Bessel functions of the mth order and ρ_s and ρ_g are respectively, the smaller and larger of ρ and a. The expression for $I(0)$ is

$$I(0) = \frac{2}{k} \int_0^{\infty} \frac{J_0(\lambda\rho)J_0(\lambda a) d\lambda}{\lambda} + \frac{4}{k} \sum_{m=1}^{\infty} \left[\cos m(\phi - z/k) I_m \left(\frac{m\rho_s}{k} \right) K_m \left(\frac{m\rho_g}{k} \right) \right]. \quad (2.14)$$

For $\alpha = 1$, we use the previous relation of Watson, in addition of the following expressions

$$\int_0^{\infty} \frac{J_1(\lambda\rho)J_1(\lambda a)}{\lambda} d\lambda = \frac{\frac{1}{2}\rho_s}{\rho_g}$$

and

$$J_{-n}(x) = (-1)^n J_n x$$

where n is the order of the Bessel function, and x is the argument of the function. The function $I(1)$ can be expressed as

$$\begin{aligned} I(1) \;=\; & \frac{1}{k} e^{i\phi} \frac{\rho_s}{\rho_g} \\ & + \frac{2}{k} \sum_{m=1}^{\infty} e^{i[(m+1)\phi - mz/k]} I_{m+1} \left[\frac{m}{k} \rho_s \right] k_{m+1} \left[\frac{m}{k} \rho_g \right] \\ & + \frac{2}{k} \sum_{m=1}^{\infty} e^{-i[(m-1)\phi - mz/k]} I_{m-1} \left[\frac{m}{k} \rho_s \right] k_{m-1} \left[\frac{m}{k} \rho_g \right] \end{aligned} \quad (2.15)$$

Equations (2.14) and (2.15), are the expressions which must be differentiated to obtain the induced velocities. In order to do this, we note the relations

$$\frac{\partial}{\partial x} = \cos\phi\frac{\partial}{\partial\rho} - \frac{\sin\phi}{\rho}\frac{\partial}{\partial\phi}, \tag{2.16}$$

$$\frac{\partial}{\partial y} = \sin\phi\frac{\partial}{\partial\rho} + \frac{\cos\phi}{\rho}\frac{\partial}{\partial\phi}. \tag{2.17}$$

Further, also note that

$$\begin{aligned}\frac{d}{d\rho}\int_0^\infty \frac{J_0(\lambda\rho)J_0(\lambda a)}{\lambda}d\lambda &= -\int_0^\infty J_0(\lambda a)J_1(\lambda\rho)d\lambda \\ &= \begin{cases}-1/\rho, & \rho>\mathrm{a} \\ 0, & \rho<\mathrm{a}\end{cases}\end{aligned}$$

Observe that there is a discontinuity at the point $\rho = a$ in derivative of the integrals, this points to fact that the velocity induced by a curvilinear vortex filament on itself is indeterminate, thus the interior and exterior velocity field to the helix must be calculated separately. The velocity field may be obtained by differentiating Eq.(2.14) and Eq.(2.15). With further algebraic manipulation, and using the relations in Eqs (2.2) and (2.17), so we have,

$$u = \frac{\Gamma}{4\pi}\left(k\left[\sin\phi\frac{\partial}{\partial\rho} + \frac{\cos\phi}{\rho}\frac{\partial}{\partial\phi}\right]I_1 - a\frac{\partial I_2}{\partial z}\right), \tag{2.18}$$

now if we define $u' = u(\Gamma/4\pi)$, and taking $\psi = \phi - z/k$, we have

$$\begin{aligned}u' = {} & \frac{4}{k}\sin\phi\sum_{m=1}^{\infty} m\cos m\psi I'_m\left(\frac{m\rho}{k}\right)K_m\left(\frac{ma}{k}\right) \\ & -\frac{4\cos\phi}{\rho}\sum_{m=1}^{\infty} m\sin m\psi I_m\left(\frac{m\rho}{k}\right)K_m\left(\frac{ma}{k}\right) \\ & -\frac{2a}{k^2}\sum_{m=1}^{\infty} m\left[\sin m\psi\cos\phi + \cos m\psi\sin\phi\right]I_{m+1}\left(\frac{m\rho}{k}\right)K_{m+1}\left(\frac{ma}{k}\right) \\ & -\frac{2a}{k^2}\sum_{m=1}^{\infty} m\left[\sin m\psi\cos\phi - \cos m\psi\sin\phi\right]I_{m-1}\left(\frac{m\rho}{k}\right)K_{m-1}\left(\frac{ma}{k}\right),\end{aligned} \tag{2.19}$$

similarly for v,

$$v = -\frac{\Gamma}{4\pi}\left(k\left[\cos\phi\frac{\partial}{\partial\rho} - \frac{\sin\phi}{\rho}\frac{\partial}{\partial\phi}\right]I_1 + a\frac{\partial I_3}{\partial z}\right), \tag{2.20}$$

if we define $v' = v(\Gamma/4\pi)$, and differentiating the Eq.(2.20)

$$\begin{aligned} v' &= -\frac{4\cos\phi}{k}\sum_{m=1}^{\infty} m\cos m\psi I'_m\left(\frac{m\rho}{k}\right)K_m\left(\frac{ma}{k}\right) \\ &\quad -\frac{4\sin\phi}{\rho}\sum_{m=1}^{\infty} m\sin m\psi I_m\left(\frac{m\rho}{k}\right)K_m\left(\frac{ma}{k}\right) \\ &\quad +\frac{2a}{k^2}\sum_{m=1}^{\infty} m\left[\cos m\psi\cos\phi - \sin m\psi\sin\phi\right]I_{m+1}\left(\frac{m\rho}{k}\right)K_{m+1}\left(\frac{ma}{k}\right) \\ &\quad -\frac{2a}{k^2}\sum_{m=1}^{\infty} m\left[\cos m\psi\cos\phi + \sin m\psi\sin\phi\right]I_{m-1}\left(\frac{m\rho}{k}\right)K_{m-1}\left(\frac{ma}{k}\right). \end{aligned} \tag{2.21}$$

Equations 2.19 and 2.21 are the components of velocity (u, v) in Cartesian coordinates. The corresponding expressions in polar coordinates can be found with the following general relations,

$$u_r = u\cos\phi + v\sin\phi,$$

and

$$u_\phi = -u\sin\theta + v\cos\theta.$$

Now, if we define $u'_r = u_r(4\pi/\Gamma)$, we get

$$
\begin{aligned}
u_r' &= \frac{4}{k}\sin\phi\cos\phi\sum_{m=1}^{\infty} m\cos m\psi I_m'\left(\frac{m\rho}{k}\right)K_m\left(\frac{ma}{k}\right)\\
&\quad -\frac{4\cos^2\phi}{\rho}\sum_{m=1}^{\infty} m\sin m\psi I_m\left(\frac{m\rho}{k}\right)K_m\left(\frac{ma}{k}\right)\\
&\quad -\frac{2a}{k^2}\cos^2\phi\sum_{m=1}^{\infty} m\sin m\psi I_{m+1}\left(\frac{m\rho}{k}\right)K_{m+1}\left(\frac{ma}{k}\right)\\
&\quad -\frac{2a}{k^2}\sin\phi\cos\phi\sum_{m=1}^{\infty} m\cos m\psi I_{m+1}\left(\frac{m\rho}{k}\right)K_{m+1}\left(\frac{ma}{k}\right)\\
&\quad -\frac{2a}{k^2}\cos^2\phi\sum_{m=1}^{\infty} m\sin m\psi I_{m-1}\left(\frac{m\rho}{k}\right)K_{m-1}\left(\frac{ma}{k}\right)\\
&\quad +\frac{2a}{k^2}\sin\phi\cos\phi\sum_{m=1}^{\infty} m\cos m\psi I_{m-1}\left(\frac{m\rho}{k}\right)K_{m-1}\left(\frac{ma}{k}\right)\\
&\quad -\frac{4}{k}\sin\phi\cos\phi\sum_{m=1}^{\infty} m\cos m\psi I_m'\left(\frac{m\rho}{k}\right)K_m\left(\frac{ma}{k}\right)\\
&\quad -\frac{4\sin^2\phi}{\rho}\sum_{m=1}^{\infty} m\sin m\psi I_m\left(\frac{m\rho}{k}\right)K_m\left(\frac{ma}{k}\right)\\
&\quad +\frac{2a}{k^2}\cos\phi\sin\phi\sum_{m=1}^{\infty} m\cos m\psi I_{m+1}\left(\frac{m\rho}{k}\right)K_{m+1}\left(\frac{ma}{k}\right)\\
&\quad -\frac{2a}{k^2}\sin^2\phi\sum_{m=1}^{\infty} m\sin m\psi I_{m+1}\left(\frac{m\rho}{k}\right)K_{m+1}\left(\frac{ma}{k}\right)\\
&\quad -\frac{2a}{k^2}\cos\phi\sin\phi\sum_{m=1}^{\infty} m\cos m\psi I_{m-1}\left(\frac{m\rho}{k}\right)K_{m-1}\left(\frac{ma}{k}\right)\\
&\quad -\frac{2a}{k^2}\sin^2\phi\sum_{m=1}^{\infty} m\sin m\psi I_{m-1}\left(\frac{m\rho}{k}\right)K_{m-1}\left(\frac{ma}{k}\right), \qquad (2.22)
\end{aligned}
$$

and simplifying

$$
\begin{aligned}
u_r &= \frac{4}{\rho}\sum_{m=1}^{\infty} m\sin m\psi I_m\left(\frac{m\rho}{k}\right)K_m\left(\frac{ma}{k}\right)\\
&\quad -\frac{2a}{k^2}\sum_{m=1}^{\infty} m\sin m\psi I_{m+1}\left(\frac{m\rho}{k}\right)K_{m+1}\left(\frac{ma}{k}\right)\\
&\quad -\frac{2a}{k^2}\sum_{m=1}^{\infty} m\sin m\psi I_{m-1}\left(\frac{m\rho}{k}\right)K_{m-1}\left(\frac{ma}{k}\right), \qquad (2.23)
\end{aligned}
$$

using the relations of the Bessel functions given by watson for I_m, K_m, Eq.(2.23) can be expanded to

$$\begin{aligned} u_r &= -\frac{a}{k^2}\sum_{m=1}^{\infty} m\sin m\psi I_{m+1}\left(\frac{m\rho}{k}\right)K_{m+1}\left(\frac{ma}{k}\right) \\ &\quad -\frac{a}{k^2}\sum_{m=1}^{\infty} m\sin m\psi I_{m-1}\left(\frac{m\rho}{k}\right)K_{m-1}\left(\frac{ma}{k}\right) \\ &\quad -\frac{a}{k^2}\sum_{m=1}^{\infty} m\sin m\psi I_{m-1}\left(\frac{m\rho}{k}\right)K_{m+1}\left(\frac{ma}{k}\right) \\ &\quad -\frac{a}{k^2}\sum_{m=1}^{\infty} m\sin m\psi I_{m+1}\left(\frac{m\rho}{k}\right)K_{m-1}\left(\frac{ma}{k}\right), \end{aligned} \tag{2.24}$$

this expression can be reduced by the multiplication of the Bessel functions I'_m, K'_m, which are

$$\begin{aligned} 2I'_v(z) &= I_{v-1}(z) + I_{v+1}(z), \\ -2K'_v(z) &= K_{v-1}(z) + K_{v+1}(z), \end{aligned}$$

where v is the order of Bessel function and z is the argument [27]. Besides exchanging u'_r by u_r this yields

$$u_r = \frac{\Gamma a}{4\pi k^2}\sum_{m=1}^{\infty} m\sin m\psi I'_m\left(\frac{m\rho}{k}\right)K'_m\left(\frac{ma}{k}\right), \tag{2.25}$$

following the same procedure, we can get the expression for u_ϕ,

$$u_\phi = \frac{\Gamma a}{k\pi\rho}\sum_{m=1}^{\infty} m\cos m\psi k'_m\left(\frac{ma}{k}\right)I_m\left(\frac{m\rho}{k}\right). \tag{2.26}$$

The component for z can be derived directly from Eq.(2.4) and Eq.(2.15), and following the procedure described above, in addition of the relations of Bessel functions of orders m,$(m+1)$ and $(m-1)$, and algebraic manipulation, we have that

$$w = \frac{\Gamma}{2\pi k} - \frac{\Gamma a}{\pi k^2}\sum_{m=1}^{\infty} m\cos m\psi k'_m\left(\frac{ma}{k}\right)I_m\left(\frac{m\rho}{k}\right), \tag{2.27}$$

Hardin observed that the components of velocity u_ϕ and w are multiplied by the same set of Bessel functions, so that he proposed to express the velocity field interior ($\rho < a$) as,

$$\begin{aligned} u_\rho &= \frac{\Gamma a}{\pi k^2} S_2, \\ u_\phi &= \frac{\Gamma a}{k\pi\rho} S_1, \\ w &= \frac{\Gamma}{2\pi k} - \frac{\Gamma a}{\pi k^2} S_1, \end{aligned} \tag{2.28}$$

where

$$\begin{aligned} S_1 &= \sum_{m=1}^{\infty} m \cos m\psi k'_m \left(\frac{ma}{k}\right) I_m \left(\frac{m\rho}{k}\right), \\ S_2 &= \sum_{m=1}^{\infty} m \sin m\psi I'_m \left(\frac{m\rho}{k}\right) K'_m \left(\frac{ma}{k}\right). \end{aligned} \tag{2.29}$$

The velocity field exterior ($\rho > a$) may be obtained in a similar manner to that shown above, the result is

$$\begin{aligned} u_\rho &= \frac{\Gamma a}{\pi k^2} S_4, \\ u_\phi &= \frac{\Gamma}{2\pi\rho} + \frac{\Gamma a}{\rho\pi k} S_3, \\ w &= -\frac{\Gamma a}{\pi k^2} S_3 \end{aligned} \tag{2.30}$$

where

$$\begin{aligned} S_3 &= \sum_{m=1}^{\infty} m \cos m\psi k_m \left(\frac{m\rho}{k}\right) I'_m \left(\frac{ma}{k}\right), \\ S_4 &= \sum_{m=1}^{\infty} m \sin m\psi k'_m \left(\frac{m\rho}{k}\right) I'_m \left(\frac{ma}{k}\right). \end{aligned} \tag{2.31}$$

2.2 Numerical model

The numerical methods that study the evolution of inviscid flow are known as vortex elements. These methods constitute a particular class in CFD, they are grid-free, and use Lagrangian coordinates. The global flow field is determinated from the induction law of the Biot-Savart, where the vortex filaments in the wake are convected by superposition of the undisturbed flow and the induced velocity field, the trailing wake is generated by spanwise variations of the bound vorticity along the blade, the shed wake is generated by the temporal variations as the blade rotate [24]. These methods are particularly used for the numerical simulation of threedimensional unsteady vortical flows of an incompressible fluid at high Reynolds number. Roughly speaking these elements are sections of a vortex tube or filament and required only where the vorticity is nonzero[25].
Fig. 2.2 shows the dynamic of a thin vortex filament given by a Frenet-Serret frame, where the local tangent vector is $t = \partial r/\partial s$, n is the principal normal, and the binormal is $b = t \times n$.

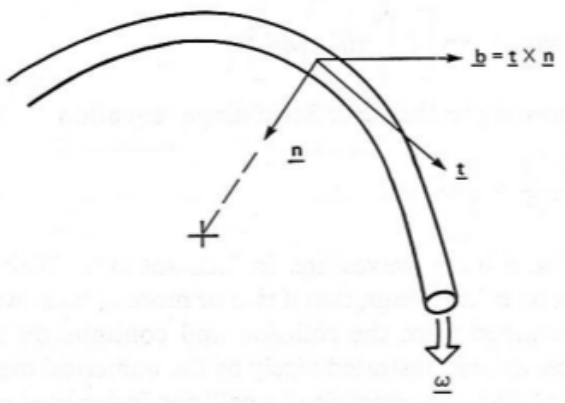

Figure 2.2: A vortex filament described by a Frenet-Serret frame

The vortex elements were developed to study the problems in aeronautics such as: the trailing vortices generated by the wing of an airplane, or the wake generated by the rotor of an helicopter. Recently, these methods have been employed to simulate the wake behind a wind turbine with good agreement.
The success of these methods in describing the flow in the wakes of horizontal axis wind turbines resides in the fact that the vorticity is confined to a narrow helical regions generated by the circular motion of the blades and the sweeping effect of the wind. Below, we present the basic ideas of the methodology on which these methods are based.
Let $\vec{u}(x,t)$ be the velocity field and $\vec{\omega}(x,t) = \nabla \times \vec{u}$ the vorticity field. We recall that the vorticity transport equation is the curl of the momentum equation then,we have for constant-density flow,

$$\frac{D\vec{\omega}}{Dt} = \vec{\omega} \cdot \nabla\vec{u} + \nu\nabla^2\vec{\omega}, \tag{2.32}$$

where $D/Dt = \partial/\partial t + \vec{u} \cdot \nabla$ and ν is the kinematic viscocity. In addition the strength or circulation Γ of the vortex tube can be defined as a surface integral over a given surface patch S,

$$\Gamma = \int_S \vec{\omega} \cdot dS, \tag{2.33}$$

because the vorticity field is solenoidal ($\nabla \cdot \vec{\omega} = 0$), the circulation is the same for all oriented surface patches that define a given vortex tube, and by the theorem of Stokes the circulation can also be expressed as a line integral over the curve λ bounding the patch S,

$$\Gamma = \int_\lambda \vec{u} \cdot d\lambda, \tag{2.34}$$

if we assume that λ moves as a material curve, then Γ is a function of time given by the integral of Eq. (2.32),

$$\frac{d\Gamma}{dt} = -\nu \int_\lambda \nabla \times \vec{\omega} \cdot d\lambda, \tag{2.35}$$

so that for an inviscid flow we have,

$$\frac{d\Gamma}{dt} = 0. \tag{2.36}$$

Thus a tube of vorticity retains its identity as it moves with the fluid, and the fluid velocity can be determined from the following relations,

$$\nabla \cdot \vec{u} = 0, \tag{2.37}$$

and,

$$\vec{\omega} = \nabla \times \vec{u}, \tag{2.38}$$

so that,

$$\nabla^2 \vec{u} = -\nabla \times \vec{\omega}, \tag{2.39}$$

and using Biot-Savart theorem, $\vec{u}$ may be expressed as

$$\vec{u}(\vec{x}) = -\frac{1}{4\pi} \int \frac{(\vec{x} - \vec{x}') \times \vec{\omega}(\vec{x}') d\vec{x}'}{|\vec{x} - \vec{x}'|^3} + \nabla\phi, \tag{2.40}$$

where ϕ is the potential associated with the homogeneous solution of (2.39) required to satisfy boundary conditions. Equation (2.40) is known as the Biot-Savart law for the

velocity field.
Although in each vortex, the vorticity is distributed over a finite core with a characteristic radius σ, for their study, the filaments are idealized as systems of spaces curves, each with zero cross-sectional area and constant circulation, for a single space curve C, the vorticity field is,

$$\vec{\omega}(\vec{x}) = \Gamma \int_C \delta[\vec{x} - \vec{r}(s')] \frac{\partial \vec{r}}{\partial s'} ds', \tag{2.41}$$

where $\vec{r}(s)$ is the space curve of the filament parameterized by arc length s, and Γ is the filament circulation. Then, if we use (2.40), we can find that the velocity field induced by this filament in an unbounded domain with no interior boundaries, is given by,

$$\vec{u}(\vec{x}) = -\frac{\Gamma}{4\pi} \int_C \frac{[\vec{x} - \vec{r}(s')] \times \dfrac{\partial \vec{r}}{\partial s'} ds'}{|\vec{x} - \vec{r}|^3}. \tag{2.42}$$

As long as the field point $\vec{x}$ does not approach within a distance σ of any part of the curve. As $\vec{x}$ approaches $\vec{r}(s)$ on the smooth space curve of the idialized vortex, $\vec{u}$ diverges as $1/|\vec{x} - \vec{r}(s)|$. For avoid this divergence; Rosenhead [25] proposed a modification of the Biot-savart law Eq. (2.40), he took account finite core effects for general application, and he arrived to the following expression,

$$\vec{u}(\vec{x}) = -\frac{\Gamma}{4\pi} \int_C \frac{[\vec{x} - \vec{r}(s')] \times \dfrac{\partial \vec{r}}{\partial s'} ds'}{(|\vec{x} - \vec{r}|^2 + \mu^2)^{3/2}}. \tag{2.43}$$

Later, Moore [25] proposed a new expression for the cutt-off the line integral, where he chose $\mu^2 = \alpha\sigma^2$, this change was included to the Rosenhead's expression, which resulted in

$$\frac{\partial \vec{r}_i}{\partial t} = -\sum_j \frac{\Gamma_j}{4\pi} \int \frac{[\vec{r}_i(\xi, t) - \vec{r}_j(\xi', t)] \times \dfrac{\partial \vec{r}_j}{\partial \xi'} d\xi'}{(|\vec{r}_i - \vec{r}_j|^2 + \alpha\sigma_j^2)^{3/2}}. \tag{2.44}$$

Eq. (2.44) is known as Rosenhead-Moore approximation, which can be used to obtain the evolution equations for the one-dimensional continua of space curves $\vec{r}_i(\xi)(i = 1, 2, ...N)$ for N filaments, the core parameters σ_j which may depend on time. In addition, it may be argued that σ_j should vary along the filament [25].

Chapter 3

Wind turbine performance

3.1 BEM

In the blade element theory (BEM), the forces on a blade element are calculated with the two dimensional aerofoil characteristics using an angle of attack determined from the incident resultant velocity in the cross-sectional plane of the element. All three-dimensional effects are ignored. The flow factors and the rotational speed of the rotor will determine the angle attack, which in turn will serve to obtain the aerofoil characteristic coefficients to calculate lift and drag forces.
Consider a turbine with N blades with tip radius R, chord c and pitch angle β measured between the aerofoil zero lift line and the plane of the disc, (see Fig. 3.1). Assume that the blades rotate at angular velocity Ω, with a wind speed U_∞, and define a and a' as induction factors tangential and axial respectively. The net tangential flow velocity experienced by the blade element is $(1 + a')\Omega r$, since that the tangential velocity of the blade element is Ωr, and the tangential velocity of the wake is $a'\Omega r$ [28].

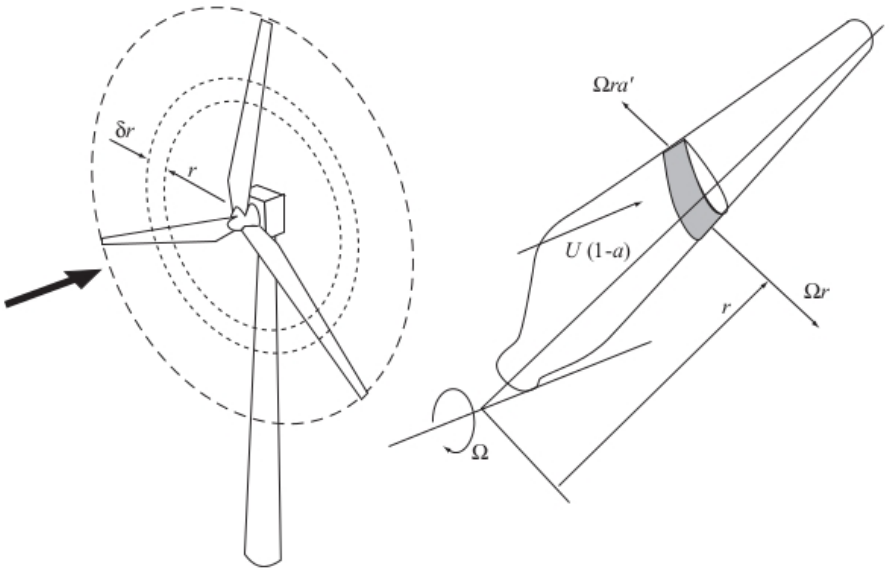

Figure 3.1: A blade element sweeps out an annular ring

Fig. 3.1, shows the diagram of velocities and forces relative to the blade,

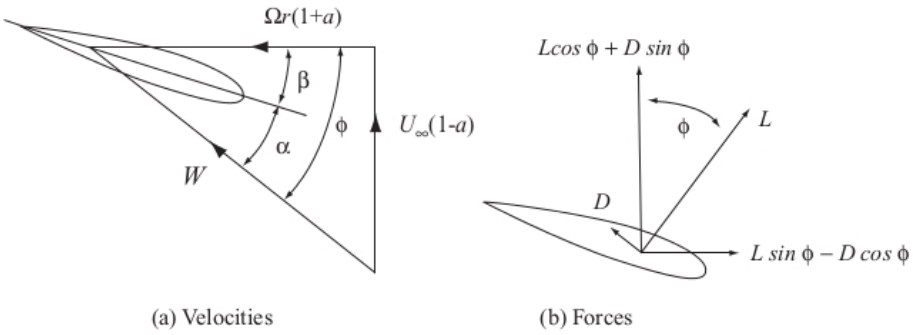

Figure 3.2: Blade element velocities and forces

from which we can define the relative velocity at the blade,

$$W = \left(U_\infty^2(1-a)^2 + \Omega^2 r^2(1+a')^2\right)^{1/2}, \tag{3.1}$$

W acts at an angle ϕ to the plane of rotation, and the following relations hold:

$$\sin\phi = \frac{U_\infty(1-a)}{W} \; and \; \cos\phi = \frac{\Omega r(1+a')}{W}. \tag{3.2}$$

From the Fig. 3.1 it can also be observed the angle attack α, is given by

$$\alpha = \phi - \beta, \tag{3.3}$$

in addition, the lift and drag forces can be defined on a span-wise length ∂r of each blade normal to the direction of W as

$$\partial L = \frac{1}{2}\rho W^2 c C_l \partial r, \tag{3.4}$$

and

$$\partial D = \frac{1}{2}\rho W^2 c C_d r \partial r. \tag{3.5}$$

The blade element momentum (BEM) theory combines both blade element theory and momentum theory, and it is used to describe the flow around blades of a turbine or propellers, it is based in the assumption of that the force on a blade element is solely responsible for the change of momentum of the air which passes through the annulus swept by the element. The BEM assumes that the axial flow induction factor does not vary radially, although in practice it is not true, the assumption is acceptable. The BEM

sets that the component of aerodynamic force on N blade elements resolved in the axial direction as

$$\partial L \cos\phi + \partial D \sin\phi = \frac{1}{2}\rho W^2 N c (C_l \cos\phi + C_d \sin\phi)\partial r, \tag{3.6}$$

and the rate of change of axial momentum of the air passing through the swept annulus as

$$\rho U_\infty (1-a) 2\pi r \partial r 2 a U_\infty = 4\pi\rho U_\infty^2 a(1-a) r \partial r, \tag{3.7}$$

moreover, the drop pressure in wake caused by the rotation is defined as,

$$P_D = \frac{1}{2}\rho(2a'\Omega r)^2, \tag{3.8}$$

and the additional axial force on the annulus is

$$\frac{1}{2}\rho(2a'\Omega r)^2 2\pi r \partial r, \tag{3.9}$$

thus

$$\frac{1}{2}\rho W^2 N c (C_l \cos\phi + C_d \sin\phi)\partial r = 4\pi\rho[U_\infty^2 a(1-a) + (a'\Omega r)^2] r \partial r, \tag{3.10}$$

simplifying

$$\frac{W^2}{U_\infty^2} N \frac{c}{R}(C_l \cos\phi + C_d \sin\phi) = 8\pi(a(1-a) + (a'\lambda\mu)^2)\mu, \tag{3.11}$$

where the parameter $\mu = r/R$.
Now, we set the element of axial rotor torque as,

$$(\partial L \sin\phi - \partial D \cos\phi) r = \frac{1}{2}\rho W^2 N c (C_l \sin\phi - C_d \cos\phi) r \partial r, \tag{3.12}$$

and the rate of change of angular momentum as

$$\rho U_\infty (1-a)\Omega r 2a' r 2\pi r \partial r = 4\pi\rho U_\infty (\Omega r) a'(1-a) r^2 \partial r, \tag{3.13}$$

so, equating the two moments

$$\frac{1}{2}\rho W^2 N c (C_l \sin\phi - C_d \cos\phi) r \partial r = 4\pi\rho U_\infty (\Omega r) a'(1-a) r^2 \partial r, \tag{3.14}$$

simplifying

$$\frac{W^2}{U_\infty^2} N \frac{c}{R}(C_l \sin\phi - C_d \cos\phi) = 8\pi\lambda\mu^2 a'(1-a). \tag{3.15}$$

If we define C_x and C_y as

$$\begin{aligned} C_x &= C_l \cos\phi + C_d \sin\phi, \\ C_y &= C_l \sin\phi - C_d \cos\phi, \end{aligned}$$

and solving the equations (3.11) and (3.15), we obtain the following equations for the induction factors,

$$\frac{a}{1-a} = \frac{\sigma_r}{4\sin\phi^2}\left[C_x - \frac{\sigma_r}{4\sin^2\phi} C_y^2\right], \tag{3.16}$$

$$\frac{a'}{1+a'} = \frac{\sigma_r C_y}{4\sin\phi\cos\phi}, \tag{3.17}$$

where

$$\sigma_r = \frac{Nc}{2\pi r} = \frac{N}{2\pi\mu}\frac{c}{R}.$$

The calculation of a and a' requires an iterative process because the two-dimensional aerodynamic characteristics are non-linear functions of the angle of attack. The iterative procedure is to assume a and a' to be zero initially, determining ϕ, C_l and C_d, and calculate new values of the flow factors. This is repeated until the convergence is achieved. The calculation of torque and power developed by a rotor needs a knowledge of a and a'. The torque is

$$Q = \frac{1}{2}\rho U_\infty^2 \pi R^3 \lambda \left[\int_0^R \mu^2 \left[8a'(1-a)\mu - \frac{W}{U_\infty}\frac{N\frac{c}{R}}{\pi} C_d(1+a')\right] d\mu\right], \tag{3.18}$$

and the power coefficients is

$$C_p = \frac{P}{\frac{1}{2}\rho U_\infty^3 \pi R^2}, \tag{3.19}$$

where $P = Q\Omega$.

3.2 Performance of a wind turbine.

The Betz limit sets that no more than 59.3% of the available energy can be extracted from the wind, but this is based on an ideal wind turbine with many assumptions and an analysis in which the rotational losses in the wake are ignored. In practice this does not happen and the performance will be reduced due to wake and tip losses, boundary layer drag, and nonideal inflow conditions. Many attempts have been made to calculate the performance of a turbine. Some models found in the literature will be described below. About a century ago, Joukowsky developed a simple aerodynamic model based on general momentum theory and the concept of a rotor disc with constant circulation, this model has since been the subject of much scrutiny researches because the power coefficient always is greater than 16/27 and for small tip-speed ratios, it tends to infinity. Although there is controvesy about this model, other have agreed that analytically the Betz limit can be exceeded, at least in theory, since the model establishes that there is no loss of efficiency associated with the rotating wake. However, numerical studies on optimum rotors have concluded that the optimum power coefficient did not exceed the Betz limit. Such that, there seems not be full agreement on the validity of the model[29]. Sørensen and van Kuik gave a possible explanation of the problem. In all analyses so far, the lateral pressure term ΔX is ignored in the momentum equation. If this term is included, the area expansion is reduced, which seems to solve the problem[30]. The wake expansion is

$$\left(\frac{R_1}{R}\right) = \frac{u}{u_1} = \frac{2\lambda q}{2\lambda q\left(1 - \frac{\Delta X}{\Delta T}\left(1 + \frac{q}{2\lambda}\right)\right) - b^2}, \tag{3.20}$$

where R_1/R is the ratio between tha wake radius and the rotor radius, $b = 1 - u_1/U_0$ is the axial wake interference factor, q is the circulation and is defined as,

$$q = -\lambda\left(\frac{R}{R_1}\right)^2 + \left(\frac{R}{R_1}\right)\sqrt{\left(\frac{R}{R_1}\right)^2\lambda^2 + b(2-b)}, \tag{3.21}$$

and the power coefficient is written as,

$$C_p = 4a(1-a)^2\frac{\lambda}{\lambda + \frac{1}{2}q}. \tag{3.22}$$

Utilizing general momentum theory Glauert developed a simple model for the optimum rotor that included rotational velocities, thus the rotor is evaluated as a rotating axisymmetric actuator disk. The main approximation of Glauert was to ignore the influence of the azimuthal velocity and the term δX in the axial moemntum[31]. Glauert derived the following equation for the power coefficient,

$$C_P = 8\lambda^2\int_0^1 a'(1-a)x^3dx, \tag{3.23}$$

where $x = r/R$ and,

$$a' = \frac{1-3a}{4a-1}. \tag{3.24}$$

In 1976 Wilson and et al., derived the following formula to estimate the power coefficient that can be achieved with a given potential rotor configuration,

$$C_{P,max} = \frac{16}{27}\lambda \left[\frac{N_b^{2/3}}{1.48 + (N_b^{2/3} - 0.04)\lambda + 0.0025\lambda^2} - \left(\frac{C_d}{C_l}\right) \frac{1.92 N_b \lambda}{1 + 2\lambda N_b} \right], \tag{3.25}$$

the model is based on a fit to Glauert's model and includes airfoil drag and the influence of a finite number of blades through the tip correction, their fit to the data is accurate to within 0.5% for tip-speed ratios from 4 to 20, drag-to -lift ratios C_d/C_l from 0 to 0.04[32]. Okulov and Sørensen in 2008 developed an analytical model to answer the question of the maximum wind kinetic energy that can be utlized by a wind turbine. Their model takes into account the rotation velocity in the wake beyond the ideal rotor with an infinite number of blades, and for this, they employed the Betz theory, as well as Goldstein theory. The C_P reported is[33],

$$C_P = 2\tilde{w}\left(1 - \frac{1}{2}\tilde{w}\right)\left(I_1 - \frac{1}{2}\tilde{w} I_3\right), \tag{3.26}$$

where

$$I_1 = 2\int_0^1 G(x,h)x dx, I_3 = 2\int_0^1 G(x,h)\frac{x^3 dx}{x^2 + l^2}. \tag{3.27}$$

Later, Okulov and Sørensen developed an analytical model for rotors with a finite number of blades and constant circulation distribution. The model was based on the work of Joukowsky, in which it the performance of wind turbine is defined as,

$$C_P = 2a\left(1 - \frac{1}{2}aJ_1\right)\left(1 - \frac{1}{2}aJ_3\right), \tag{3.28}$$

where

$$J_1 = 1 + \sigma, J_3 = 2\int_0^1 \tilde{u}_z(x,0)x dx. \tag{3.29}$$

In addition, they compared the previous models, and they found that the Joukowsky rotor achieves a higher efficiency than the Betz rotor, but the efficiency of the Betz rotor is larger if we compare it for the same deceleration of the wind speed[21].
Wood and et al. in 1991 developed a novel expression to calculate the performance of wind turbine, in which the trailing vorticity in the far-wake was represented by a number

of vortex lines and the velocities induced at the blades were found using the Biot-savart law. The novel features of this method are based on the equations derived for the averages velocities in the far-wake. In addition, by proceeding outwards from the hub vortex, the wake is assembled iteratively by balancing the angular and axial momentum fluxes in each streamtube against the torque and thrust, respectively, acting on the relevant blade element. The expression for C_P is defined as,

$$C_P(k) = XNU_\infty(k)\Gamma_k\Delta r_\infty^2(k)/\pi, \tag{3.30}$$

where k refers to the streamtube, X is the tip speed ratio, N is the number of blades, U_∞ is the axial velocity in the far wake, Γ_k is the bound circulation of the each blade element, and $\Delta r_\infty^2(k)$ is the streamtube area in the far-wake[34, 35]. Thereupon, Wood presented a new study for wind turbines at high tip speed ratios, he modeled the trailing tip vortices as an infinite row of vortex rings. This formulation avoided the use of average velocities and yielded thrust and energy equations that involve the axial velocity of the trailing vortices. In this analysis, the performance of the wind turbine is calculated as,

$$C_P = 2U_V(1 - U_\infty)U_\infty R_\infty^2, \tag{3.31}$$

where, $U_V = (1 + U_\infty)/2$, R_∞ is the radius of the tip vortex, and U_∞ is the average axial velocity in far-wake[36]. Finally he published a new study, which he included swirl to the actuator disk analysis in the wake of a wind turbine. It was shown that swirl in the wake of a wind turbine does not have a significant effect on the basic analysis that lead to the Betz limit provided that the core radius of the hub vortex is sufficiently small and the tip speed ratio is sufficiently high. The key feature of the analysis was the demonstration that the structure of the vortex wake behind the rotor can have a major impact on turbine performance, which it is,

$$C_P = \frac{1}{2}\left(1 - U_\infty^2\right)(1 + U_\infty)\left[1 + \frac{1 - U_\infty^2}{\lambda^2}\{ln(1/a_1) - 1/2\}\right], \tag{3.32}$$

if $\lambda \to \infty$ we recover the standard equation for C_P that leads to the Betz limit[37].

3.3 Rankine vortex model

As we have seen in the previous section several studies about the C_P have been developed, and also that the trend is to include the effects of the wake in the calculation of the performance of the wind turbine, such as: swirl; instabilities, dissipation, and expansion of the wake. Unfortunately, the lack of data of the velocity field behind of a wind turbine makes it difficult the validation of the models.
We have based our analysis of the performance of a wind turbine on the model developed by Tavares and et al. [38]. The original Tavares model optimizes the distribution of chord and twist angle of horizontal axis wind turbines by taking into account the influence of the wake which is considered a Rankine vortex. The optimization is based on maximizing the power coefficient coupled with the general relationship between the axial induction factor in the rotor plane and in the wake. Fig. 3.3 illustrates the behavior of the flow in a streamtube and the flow axial velocities.

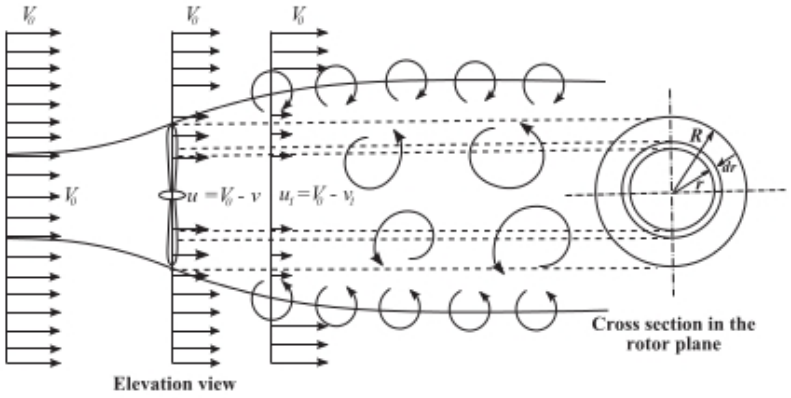

Figure 3.3: Illustration of the velocities in the rotor plane and in the wake

Wilson and Lissaman presented a mathematical model that realtes the induction factors with the induced velocities[39], namely

$$a = \frac{V_0 - u}{V_0}, \tag{3.33}$$

$$b = \frac{V_0 - u_1}{V_0}, \tag{3.34}$$

where a is the axial induction factor in the rotor, b is the axial induction factor in the wake, V_0 is the velocity of undisturbed flow, u and u_1 are the induced velocities in the rotor plane and in the wake respectively, that are defined as,

$$V_0 - v = u \equiv (1-a)V_0,$$
$$V_0 - v_1 = u_1 \equiv (1-b)V_0, \tag{3.35}$$

the power coefficient has the form,

$$C_P = \frac{b^2(1-a)^2}{b-a}, \tag{3.36}$$

in addition, Mesquita and Alves showed that the tangencial induction factors a' in the rotor, and b' in the wake [40], can be defined as

$$a' = \frac{w}{2\Omega}, \tag{3.37}$$

$$b' = \frac{w_1}{2\Omega}, \tag{3.38}$$

where Ω is the angular speed of the wind turbine, w and w_1 are the rotor and wake angular velocities of the fluid. Wilson and Lissaman showed that it is possible to establish a relationship between the axial induction factors a and b [39], by the aplication of the continuity, momentum, and energy equations in the streamtube shown in the Fig. 3.3, this relationship is

$$a = \frac{b}{2}\left[1 - \frac{b^2(1-a)}{4X^2(b-a)}\right], \tag{3.39}$$

where X is the tip speed ratio, defined by,

$$X = \frac{R\Omega}{V_0}. \tag{3.40}$$

Mesquita and Alves showed that Eq. 3.39 can be rearranged in the form of a cubic equation for b, where only one of the roots has a consistent behavior with the physical of the problem[40]. The expression is

$$b = -\frac{1}{2}(S+T) - \frac{1}{3}a_1 - i\frac{1}{2}\sqrt{3}(S-T), \tag{3.41}$$

where,

$$S = \sqrt[3]{Z + \sqrt{Q^3 + Z^2}}, \tag{3.42}$$

$$T = \sqrt[3]{Z - \sqrt{Q^3 + Z^2}}, \tag{3.43}$$

$$Q = \frac{3a_2 - a_1^2}{9}, \tag{3.44}$$

$$Z = \frac{9a_1a_2 - 27a_3 - 2a_1^3}{54}, \tag{3.45}$$

$$a_1 = \frac{4X^2}{a-1}, \tag{3.46}$$

$$a_2 = \frac{12aX^2}{1-a}, \tag{3.47}$$

$$a_3 = \frac{8a^2X^2}{a-1}, \tag{3.48}$$

To improve their model, Wilson and Lissaman had included the effect of the wake in their analysis with the hypothesis of free vortex, but they realized that this assumption causes infinite velocities in the wake near to the axis of the wind turbine[39]. For this reason, they decided to use a Rankine vortex instead of the irrotational vortex to represent the wake, which solves the problem of infinite velocities. This approach introduces a parameter $N = \Omega/w_{max}$ in the Eq. (3.36), which results in,

$$C_P = \frac{b(1-a)^2}{b-a}[2Na + (1-N)b]. \tag{3.49}$$

Tavares et al. carried out an aerodynamic optimization of the chord and twist angle, by maximizing the power coefficient given by Eq. (3.49), making $dC_P/da = 0$, resulting in the expression

$$\begin{aligned} &2\frac{db}{da}Na^3 + 2\left\{2bN - \frac{db}{da}[b(N-1)+N]\right\}a^2 + \\ &\left\{2b\frac{db}{da}(N-1) + b^2\left[1 - 7N + \frac{db}{da}(N-1)\right]\right\}a \\ &\quad b^2\left[1 - \frac{db}{da}(N-1) + N\right] + 2b^3(N-1) = 0. \end{aligned} \tag{3.50}$$

Dividing the last equation by $2Ndb/da$ gives,

$$a^3 + \delta_1 a^2 + \delta_2 a + \delta_3 = 0, \tag{3.51}$$

where,

$$\delta_1 = \frac{2bN - \frac{db}{da}[b(N-1)+N]}{N\frac{db}{da}}, \tag{3.52}$$

$$\delta_2 = \frac{2b\frac{db}{da}(N-1) + b^2\left[1 - 7N + \frac{db}{da}(N-1)\right]}{2N\frac{db}{da}}, \tag{3.53}$$

$$\delta_3 = \frac{b^2\left[1 - \frac{db}{da}(N-1) + N\right] + 2b^3(N-1)}{2N\frac{db}{da}}, \tag{3.54}$$

and db/da is,

$$\frac{db}{da} = \frac{8a^2X^2 - b\{16aX^2 - b[b(1-b) + 8X^2]\}}{4a^2X^2 + b\{-8aX^2 + b[3a(1-a) - 2b(1-a) + 4X^2]\}}. \tag{3.55}$$

Moreover, we can note that Eq. (3.50) is a cubic equation in a, where only one root has a physically consistent solution, this solution is given by,

$$a_{opt} = -\frac{1}{2}(S_* + T_*) - \frac{1}{3}\delta_1 - i\frac{1}{2}\sqrt{3}(S_* - T_*), \tag{3.56}$$

where,

$$S_* = \sqrt[3]{Z_* + \sqrt{Q_*^3 + Z_*^2}}, \tag{3.57}$$

$$T_* = \sqrt[3]{Z_* - \sqrt{Q_*^3 + Z_*^2}}, \tag{3.58}$$

$$Q_* = \frac{3\delta_2 - \delta_1^2}{9}, \tag{3.59}$$

$$Z_* = \frac{9\delta_1\delta_2 - 27\delta_3 - 2\delta_1^3}{54}. \tag{3.60}$$

Therefore, with these equations we can develop an iterative procedure for the optimum aerodynamic design. The optimum chord is,

$$C_{opt} = \frac{4\pi rbFsin^2\phi}{BC_n(1 - a_{opt})} \tag{3.61}$$

where F is the tip loss factor, B is the number of blades, and $C_n = C_L\cos\phi + C_D\sin\phi$. For calculation of a', it is used the following relationship,

$$a'_{opt} = a_{opt}\frac{tan\phi}{x}, \tag{3.62}$$

with x equal to,

$$x = \frac{wr}{V_0} \tag{3.63}$$

where r is the radius of the blade element, w is the angular velocity on the rotor, and V_0 the velocity upstream. Once a'_{opt} is obtained, we can calculate b'_{opt}, which it is given by,

$$b'_{opt} = b\frac{a'_{opt}}{a_{opt}}, \tag{3.64}$$

the optimum twist angle is,

$$\beta_{opt} = \phi_{opt} - \alpha, \tag{3.65}$$

where ϕ_{opt} is given by,

$$\phi_{opt} = tan^{-1}\left[\frac{(1 - a_{opt})}{1 + a'_{opt}x}\right]. \tag{3.66}$$

The iterative procedure requires the folowing input data: Ω, r, α, $C_L(\alpha)$, $C_D(\alpha)$ and V_0, in addition to set initial values to a and a'. The stop criterium is given by comparing the error calculated from the difference between the previous and current Cp with a given tolerance.

Chapter 4

Results

In this chapter, the results will be presented in five different parts. In part one, the velocity field obtained from Hardin model, as well as the behavior of the velocity components in a section of the control volume are described. In part two, the numerical solution of the velocity fied generated by the helical vortices and the comparison with the analytical model and other case studies are presented. In part three, an study of consistency of the analytical and numerical models is presented. In part four, the behavior of the BEM with the Rankine vortex wake according to the model of Tavares [38] is presented. Finally, in part five, the results obtained from the BEM with the Rankine vortex, but including the average velocities calculated in the wake proposed in this study are discussed.

4.1 Analytical model

In this section we study the model developed by Hardin [8]. We focus on two different cases of study. First we study the case of an advance equal to one, ie $2\pi k = 1$. And then, we describe the dynamics for an advance equal to six ($2\pi k = 6$).
Fig. 4.1 shows the azimuthal velocity $U\phi$ as a function of the radial coordinate taking ϕ as a parameter. In this we can see that $U\phi$ has small values when the advance is equal to one. Also we can see that as we move away from origin, the magnitudes of the velocity begin to grow up in absolute value to the last point calculated ($\rho = 0.9$). This indicates that the magnitudes become bigger because near the edge the influence of the filament which generates the velocity field is larger.

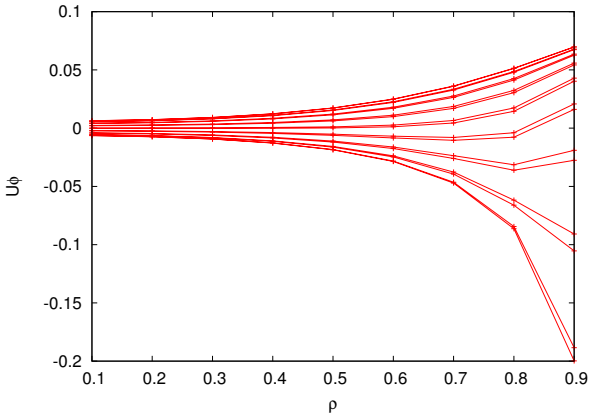

Figure 4.1: Azimuthal velocity ($U\phi$) as a function of ρ, with $2\pi k = 1$. The uppermost line is at $\phi = 5.585$ rad and the ϕ increment between lines is 0.349 rad.

Fig. 4.2 shows the radial velocity as a function of ρ, where we can observe that the radial velocity near the center of the field is small, and when we move to a larger ρ, it increases. We note that $U\rho$ near of the origin has the same magnitudes of the velocity for different ϕ, and when ρ approaches to the edge the values of $U\rho$ vary as a function of ϕ. The magnitudes of $U\rho$ are bigger than those shown by $U\phi$. Moreover, in the same way of $U\phi$ when ρ approaches to a the magnitudes of $U\rho$ becomes bigger, which could again be due to the large influence of the vortex filament. Also $U\rho$ shows a behavior more symmetric than $U\phi$, which it is expected.

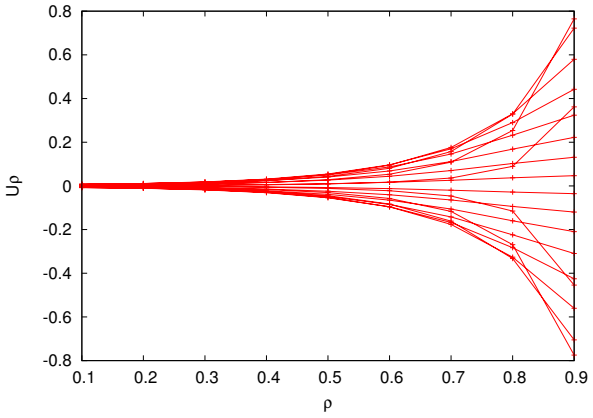

Figure 4.2: Radial velocity ($U\rho$) as a function of ρ, with $2\pi k = 1$. The uppermost line is at $\phi = 1.047$ rad and the ϕ increment between lines is 0.349 rad.

Fig. 4.3 presents the axial component of the velocity as a fucntion of the radial coordinate ρ, it shows that Uz has larger magnitudes that $U\phi$ and $U\rho$. This is expected, because the filament is tight enough, which effectively results in the approximate formation of a

vortex tube with fluid moving inside, mostly in the axial direction. As we move away from the center towards the edge, we see that the axial velocity varies with ϕ, in some cases it becomes bigger than value initial, and in others it becomes lower.

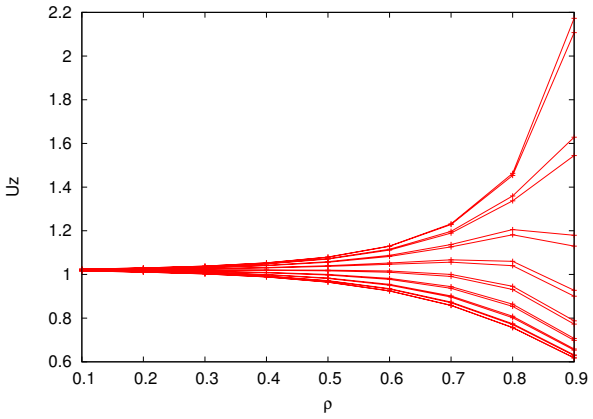

Figure 4.3: Axial velocity (Uz) as a function of ρ, with $2\pi k = 1$. The uppermost line is at $\phi = 2.443$ rad and the ϕ increment between lines is 0.349 rad.

The three components of the velocity obtained with the analytical model have approximately the same magnitudes near of the origin even at different ϕ. And then, as we move on ρ, their relative magnitudes become different. $U\rho$ has a symmetrical behavior, and $U\phi$ and Uz have a symmetrical behavior in some regions, especially when ρ is lower than 0.6. But near the edge $U\phi$ and Uz have some values that vary from the rest, and this can be due to the presence of the filament.
The velocity field obtained from the analytical model with advance of one ($2\pi k = 1$) is shown in Fig. 4.4. Two major features of the velocity field can be distinguished. In the vicinity of the vorticity filament, the velocity field rotates around the filament, as expected. Since the filament coils six times in a limit length, six vortical structures are displayed near the upper and lower edges of the cluster of vectors. Fig. 4.4 also shows that the velocity field in the center is more intense than at the edge. Except for those points that describe the helix, where the velocity components are larger, these give the impression that the helix interacts with the exterior field ($\rho > a$, where a is the radius of the filament, see section 2.1).

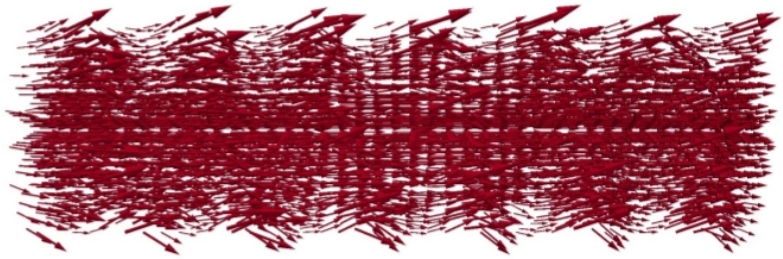

Figure 4.4: Side view of the velocity field with an advance of $2\pi k = 1$.

Figure 4.5: A view of the edge of the velocity field with an advance of $2\pi k = 1$.

We describe now the behavior of the velocity field obtained with the analytical model for an advance equal to six ($2\pi k = 6$), in which the filament is more expanded. Fig. 4.6 shows the azimuthal velocity $U\phi$ as a function of ρ, where we can see that the azimuthal component has magnitudes larger than those observed for $U\phi$ with advance of one. In addition, the figure shows that when ϕ has the values of 1.396 and 5.584 rad, $U\phi$ almost does not vary in its value. At the top of the graph near 0.2, we can see that there are values of ϕ (0.349, 6.282, 0.698, 5.933, 1.047) that behave in the same way and these reduce to a value of approximately 0.1, this is the behavior that we observe more markedly. It is observed that all values of $U\phi$ start between -0.2 and 0.2, and almost all remain in this range. But the lower line of $U\phi$ becomes larger towards negative values when r approaches to the edge, this could be due to the presence of the filament or the lack of convergence of the series for some ϕ, the same behavior was noted for an advance equal to one.

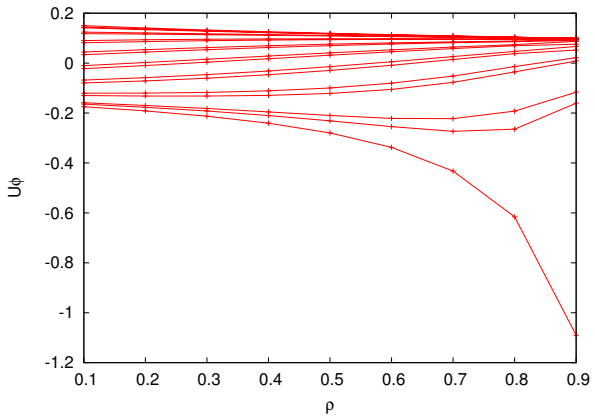

Figure 4.6: Azimuthal velocity ($U\phi$) as a function of ρ, with $2\pi k = 6$. The uppermost line is at $\phi = 0.349$ rad and the ϕ increment between lines is 0.349 rad.

Fig. 4.7 shows the behavior of the radial component of the velocity as a function of r. Its magnitudes range from -0.2 to 0.2, also we can see a more symmetric behavior than the azimuthal component. We can observe that the magnitudes of the velocity do not vary up to ρ equal to 0.4, but after this its values are slightly larger or smaller depending on ϕ. It is noticed that there are two values of ϕ, for which the $U\rho$ component increases or decreases to 0.6 or -0.6 respectively.

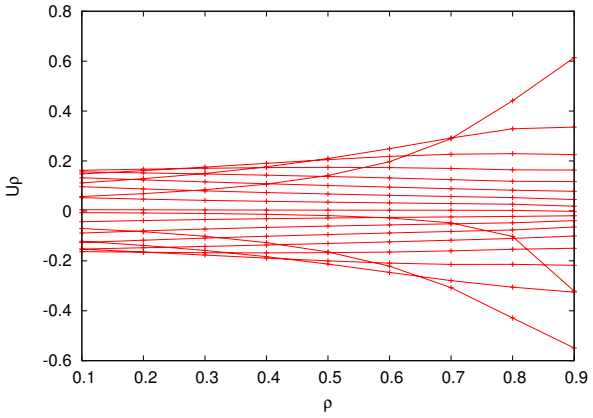

Figure 4.7: Radial velocity ($U\rho$) as a function of ρ, with $2\pi k = 6$. The uppermost line is at $\phi = 3.141$ rad and the ϕ increment between lines is 0.349 rad.

In Fig. 4.8, we show the axial component of the velocity as a function of ρ. As it can be observed that all the magnitudes of the velocity are positive. It also shows that for different values of ϕ, Uz behaves in a similar way, and only some values of ϕ move away from the set that begins in a value of 0.2 and ends about 0.1. Further we can see again as Uz grows for a given ϕ, as we approach the edge, perhaps this is due to the presence of the filament. In Fig. 4.8 can be noted as the behavior of Uz seems to be inversely proportional to the behavior shown by $U\phi$, being consistent with what it happens when we have an advance of one.

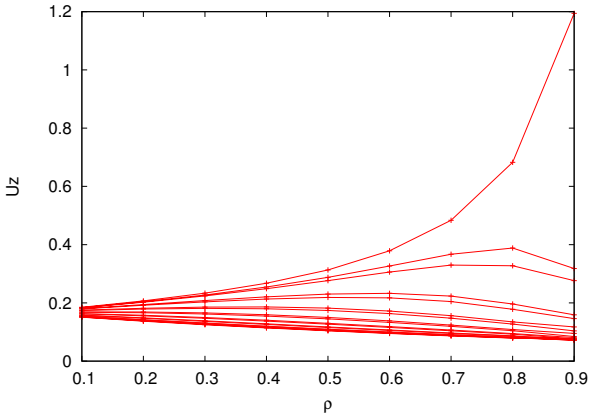

Figure 4.8: Axial velocity (Uz) as a function of ρ, with $2\pi k = 6$. The uppermost line is at $\phi = 3.49$ rad and the ϕ increment between lines is 0.349 rad.

From the graphs presented previously, we can observe that $U\rho$ and $U\phi$ have similar values, close between -0.2 to 0.2, and Uz at values near 0.2 for small ρ ($\rho < 0.4$). This indicates that when the advance is equal to six, the components of the velocity $U\phi$ and $U\rho$ gain importance, ie. the velocity generated by the filament it is distributed among all components, and this is because the filament is sufficiently extended. Another important feature is that $U\phi$ and Uz have values of ϕ where they grow more than it is expected.
Fig. 4.9 shows a side view of of the velocity field obtained with advance of six. We can see that the velocity field tends to be more intense and approximately aligned with the vortex filament. Also, we see that there is a single coil in advance of six in the domain of 2π. For this advance, we can see that there is an increase in $U\phi$ and $U\rho$, in contrast to what it was shown with an advance equal to one, where the field is dominated by the axial component.

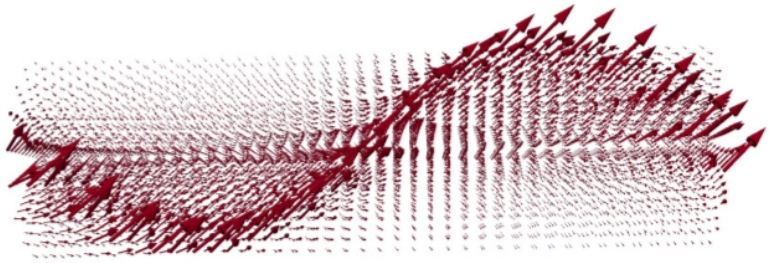

Figure 4.9: Side view of the velocity generated by a filament, with advance of six.

The graphs presented above show that the velocity field is strongly influenced only in the vicinity of the filament, where the vectors are oriented approximately parallel to the helical vortex. Away from it the vectors are not strongly influenced.
It is important to observe the behavior of the analytical model in the exterior velocity field

($\rho > a$), namely when ρ is bigger than a, which is the diameter of the filament. Fig. 4.10 shows that when we have an advance of one, the velocity field tends to be more intense in the interior field ($\rho < a$). Only on the border between the interior and exterior field, the exterior field is influenced by the filament. this indicates that there is conservation of mass for $2\pi k = 1$. Fig 4.11 shows the behavior of Hardin's model with an advance equal to six, in this we can see that the filament has an increased interaction with the exterior field, although it is slight with the vectors that are located away of the vortex. Again, it shows that the bigger vectors are in the vicinity of the filament, including those that are located on the external field.

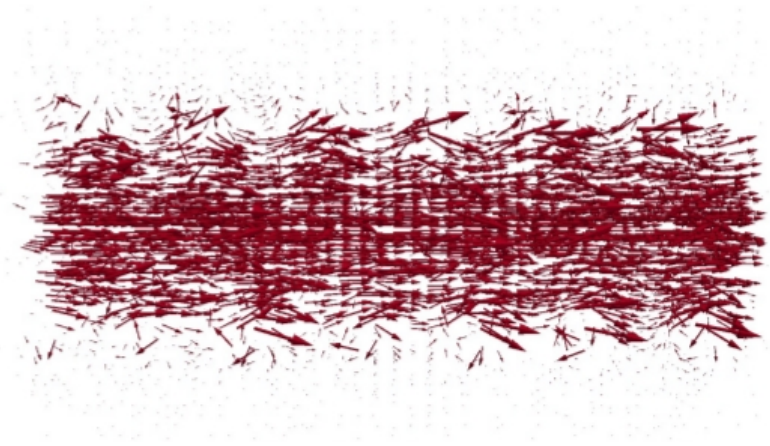

Figure 4.10: Side view of the exterior and interior velocity field generated by a filament with an advance of one.

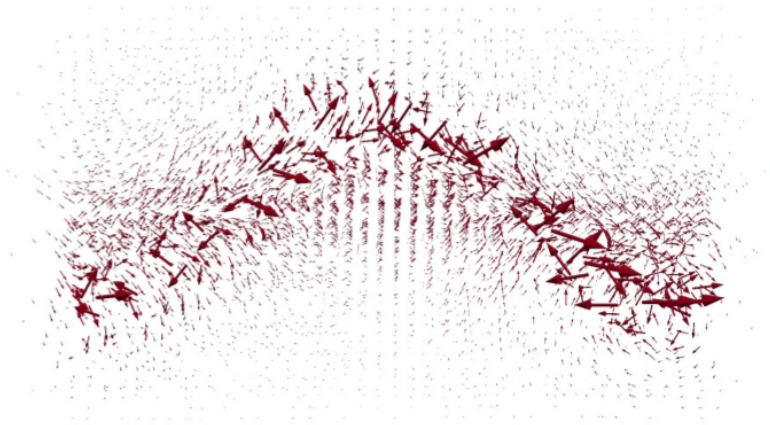

Figure 4.11: Side view of the external and interior velocity field generated by a filament with an advance of six.

The study of the different advances is of great importance, because these have a direct

influence on the design of the wind turbines. As we saw in the graphs above, the phenomenon changes as a function of the advance. When the advance is equal to one, the interior velocity field moves almost as a rigid body. Also we can see that for an advance equal to six, the wake does not move as a whole, the vorticity tends to be preserved in the filament and its surroundings.

4.2 Numerical model

Fig. 4.12, shows the azimuthal velocity as a function of the radial coordinate ρ. We see that the magnitude of $U\phi$ is small, but slightly larger than those obtained with the analytical model (see, Fig. 4.1). Also, we note that there is a qualitative similarity between the corresponding traces of the two models. Since as ρ tends to larger values, $U\phi$ becomes larger in both cases, though quantitatively they do not coincide. This might be due to different scaling. The curves of Fig. 4.12 are symmetric, which it is expected for tight enough coiled filaments.

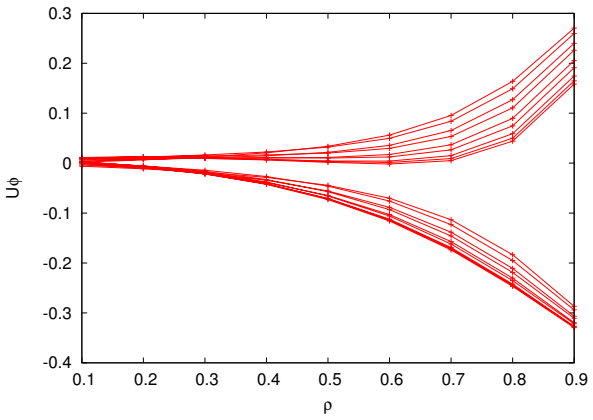

Figure 4.12: Azimuthal velocity ($U\phi$) as a function of ρ, with $2\pi k = 1$. The uppermost line is at $\phi = 1.396$ rad and the ϕ increment between lines is 0.349 rad.

Fig. 4.13 shows the radial velocity as a function of ρ. The velocity near the origin is almost the same for different ϕ, and as we approach the edge $U\rho$ varies with ϕ. The magnitudes of $U\rho$ are slightly higher than those presented by $U\phi$, we can also observe that this component has a more symmetrical behavior. When we compare Fig. 4.13 with Fig. 4.2, we see that are quantitatively close to each other, the numerical solution has values ranging from -1 to 1, whereas in the analytical solution ranging from -0.8 to 0.8. Further, we can see that the behavior is very similar, thus presenting a qualitative similarity.

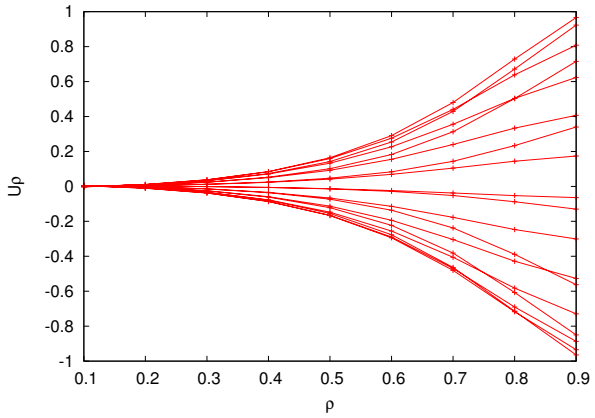

Figure 4.13: Radial velocity ($U\rho$) as a function of ρ, with $2\pi k = 1$. The uppermost line is at $\phi = 4.886$ rad and the ϕ increment between lines is 0.349 rad.

Fig. 4.14 shows the axial component of the velocity Uz as a function of ρ. The magnitudes of Uz are large near of the origin, and as we approach the edge it decreases. Also, unlike the rest of the components, it diminishes for all values of ϕ, as soon as we approach $\rho = 0.9$. The magnitudes of Uz are larger than the other two components, with values ranging from 5.4 to 3.1. When we compare Fig. 4.14 with Fig. 4.3, we note that the analytical model has smaller magnitudes of the velocity than those presented by the numerical model, ie there is no quantitative agreement, which we could indicate again that may be a problem of scale in any of the models. For certain values of ϕ, we can see that there is some agreement in the behavior of Uz, thus it shows some qualitative similarity.

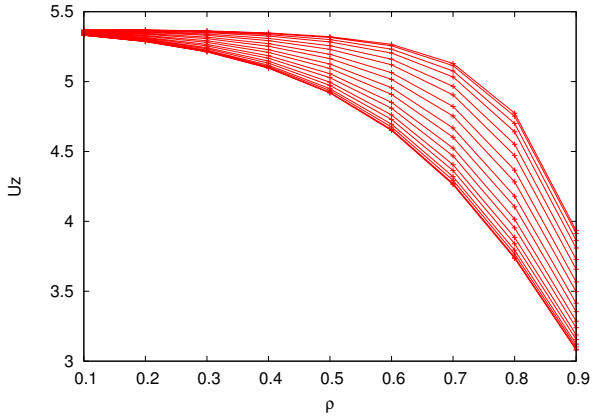

Figure 4.14: Axial velocity (Uz) as a function of ρ, with $2\pi k = 1$. The uppermost line is at $\phi = 6.282$ rad and the ϕ increment between lines is 0.349 rad.

The behavior of the three components of the numerical model is symmetrical, which is expected for filament with tight enough coils. Although Uz shows a strange behavior by

telling us that the axial velocity is more intense at the origin away from the filament. This behavior is not clear to us, and we believe that further research is needed on the subject. It is easy to see that there is not much quantitative agreement between the models, but qualitatively there is certain agreement in some regions.
Now, we describe the behavior of the velocity field obtained by the numerical method, in which the helical votex is not coupled to the velocity field, so its behavior can be observed in more detail. In this type of simulation is necessary to generate the filament, from which we obtain the velocity field. Below we present the graphics obtained from the simulation for a helical votex with an advance equal to one, a domain of 2π, and with a number of coils equal to six. In Fig. 4.15, we see a side view of the helical vortex filament, where we can observe that for an advance of one, the velocities on the filament are influenced by each other. If the filament is compressed enough the velocities at a point on the vortex filament will be strongly influenced by the velocities of the subsequent coils, which causes that the filament to move as a solid, at a constant velocity.

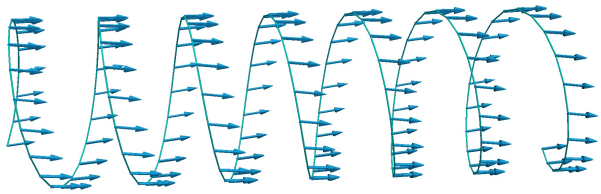

Figure 4.15: Side view of the helical vortex filament.

Fig. 4.16 shows a isometric view of the helical vortex filament, in which we can observe a homogeneous behavior of the filament again. Also we can note that the magnitudes of the velocity over the filament are constant. Namely, it does not show an increase in the angular momentum in the filament for an advance of one, as shown in Hardin's model. The numerical method shows that for this advance, the filament does not seem to have influence on the external region ($\rho > a$), unlike Hardin model where a slight inference can be detected.

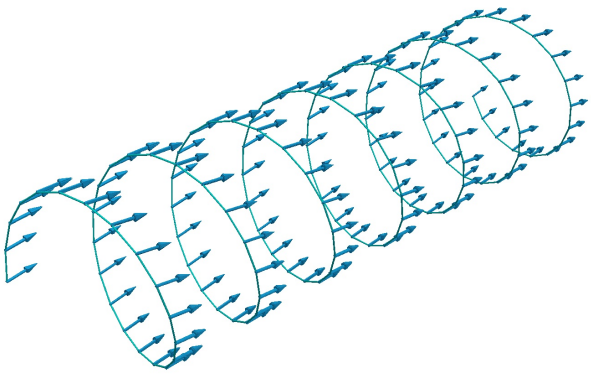

Figure 4.16: Isometric view of the helical vortex filament.

Fig. 4.17 shows a side view of the velocity field generated by the vortex filament and obtained with the numerical method, where we can see that the velocity field is more uniform near of the origin, and is predominant in the axial component. But we can also see that in the edge, six regions with large vorticity are formed. This behavior describes the influence of the filament on the field, because the filament turns six times in a domain of 2π. In this view we can see that the velocity field generated by both methods, has similarities: first, the two models show that the components of the velocity field is more intense at the center. Second, the formation of regions of large vorticity on the edge, in the vicinity of the filament. Unfortunately, the interference of the filament in the Hardin's model does not allow us to observe the internal field alone.

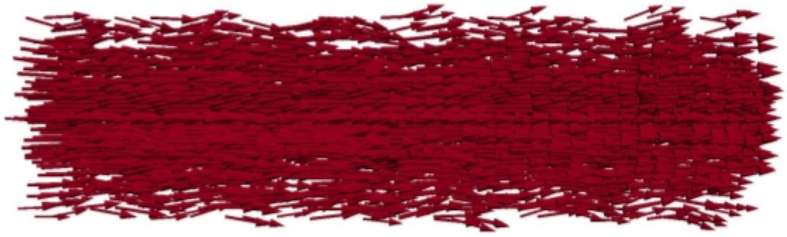

Figure 4.17: Side view of the velocity field with and advance equal to $2\pi k = 1$.

Figure 4.18: A view of the edge of the velocity field obtained from the numerical model, with an advance of $2\pi k = 1$.

In general, we observe that for an advance equal to one, the velocity field generated by both models shows qualitative consistency with each other, especially in the regions closest to the origin. The larger difference between one model and other, it is seen in regions away from the origin. The analytical model shows that near the edge, the velocity components are not only dominated by the axial velocity, they show a significant increase in the other directions of the velocity. In contrast, the numerical model shows that near the edge, the velocity field is still dominated by the motion in the axial direction.
Fig. 4.19 shows the behavior of the azimuthal velocity as a function of ρ, where we can see that $U\phi$ is in a range of values from -0.1 from 0.3, which become larger or smaller as ρ increases, taking ϕ as a parameter. Fig. 4.19 shows that $U\phi$ has different trends. The first, where a set of lines converge to values of approximately of 0.2. In the second, the lines at the top of the graph, which display an initial growth, then they seem to reach a maximum. The third includes lines mostly at the bottom of the graph, these have high initial values of $U\phi$, and as ρ becomes larger, they begin to fall to lower values, even for some lines $U\phi$ becomes negative. Only the second type of trend matches qualitatively with the analytical solution.

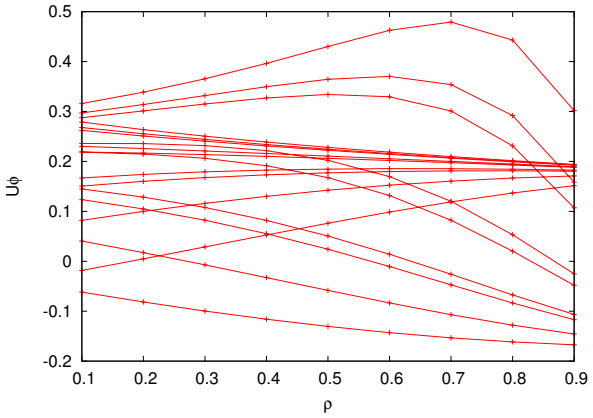

Figure 4.19: Azimuthal velocity ($U\phi$) as a function of ρ, with $2\pi k = 6$. The uppermost line is at $\phi = 3.49$ rad and the ϕ increment between lines is 0.349 rad.

Fig. 4.20 shows the behavior of the radial velocity $U\rho$ as a function of ρ, in which we can see that this component presents a more symmetrical behavior than it was shown by $U\phi$. We see that $U\rho$ has initial values ranging from -0.3 to 0.3, and these remain in this range practically up to $\rho = 0.4$, except for the outer lines. When we compare Fig. 4.20 with the results obtained with the analytical model (see Fig. 4.7), we note that the both models have a set of lines begin in the interval -0.2 and 0.2. The models are in qualitative agreement. Also, in both cases the set of lines expand when ρ becomes larger. Furthermore, the outer lines show a similar final value ($\rho = 0.9$).

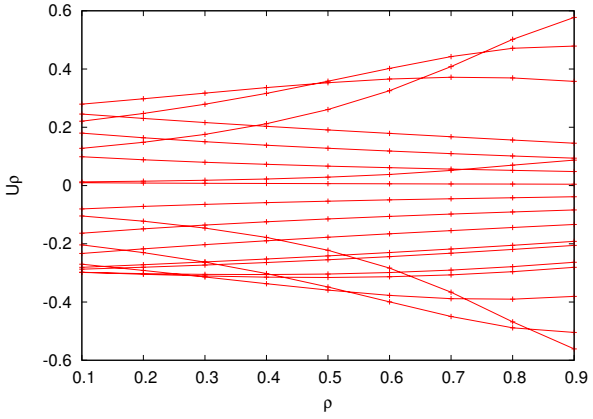

Figure 4.20: Radial velocity ($U\rho$) as a function of ρ, with $2\pi k = 6$. The uppermost line is at $\phi = 3.839$ rad and the ϕ increment between lines is 0.349 rad.

The axial component Uz as a function of ρ is shown in Fig. 4.21, where we note that Uz initially has values between 0.25 to 0.35, and as ρ becomes larger these values vary, depending of value ϕ. These become larger or smaller, also can be observe that for all values

of ϕ, Uz is positive. The three lines that are on the top on the graph reach a maximum and then fall. While the lower ones are monotonously decresing. the bottom a set of lines falls from the beginning toward lower values of 0.3. In middle section we can observe that there is a combination of the two trend just described. When we compare the analytical and numerical models, we can see that there is a certain qualitative agreement, in the central part of the set of lines, and in the outer lines since the same behavior is exhibited in both cases, but the top line of the analytical model reaches larger values them those of the numerical model.

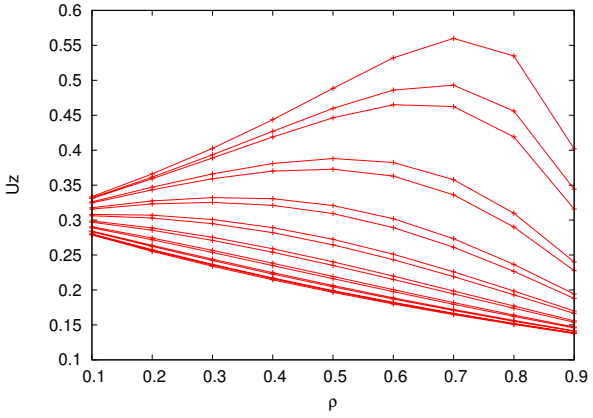

Figure 4.21: Axial velocity (Uz) as a function of ρ, with $2\pi k = 6$. The uppermost line is at $\phi = 3.49$ rad and the ϕ increment between lines is 0.349 rad.

With the advance of $2\pi k = 6$ the filament is more expanded than in the previous example taking only one turn in the 2π domain. Fig. 4.22 shows a side view of the helical vortex. The vectors on the right hand half of the filament point upward with a small angle, and in the second half the velocity vectors point downward with an angle of the same absolute value. This behavior indicates that the helical vortex moves forward.

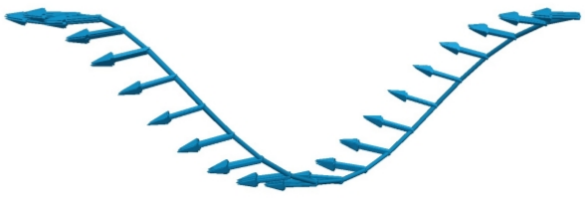

Figure 4.22: Side view of the filament, with an advance of 6.

The velocity field produced by the filament can be seen in Fig. 4.23 which shows a side view of velocity field. The velocity vectors located in the vicinity of the filament are more intense while the velocity vectors far from the filament are not very influenced by its

presence. The velocity distribution is similar to that obtained with the analytical solution. This suggests that there is qualitative consistency between models, but we can see that the field generated by the numerical solution is more intense, indicating a difference in scale between both models.

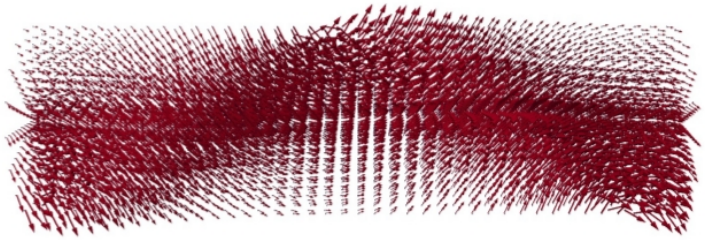

Figure 4.23: Side view of the velocity field generated by a filament, with an advance of six.

The velocity field obtained with an advance equal to six shows that it tends to follow the velocity field on the filament, and this can be observed both the analytical and numerical model. It was also observed that now the field is not only dominated by the axial component, unlike what happens with an advance equal to one. Further, when the filament is expanded, it has not a major influence on the entire field, only on the neighbouring region. Fig. 4.24 and Fig. 4.25 show the exterior and interior velocity field obtained from the numerical model which are according to shown by the analytical model. With the only difference that the velocity fields obtained from the numerical solution are more intense.

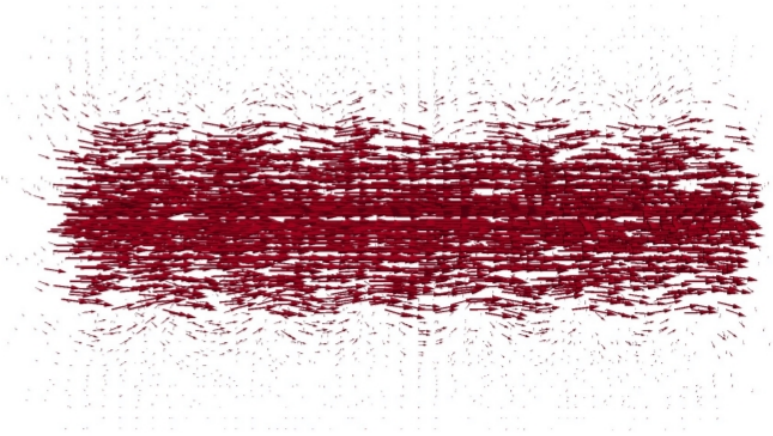

Figure 4.24: Side view of the exterior velocity field generated by a filament with an advance of one.

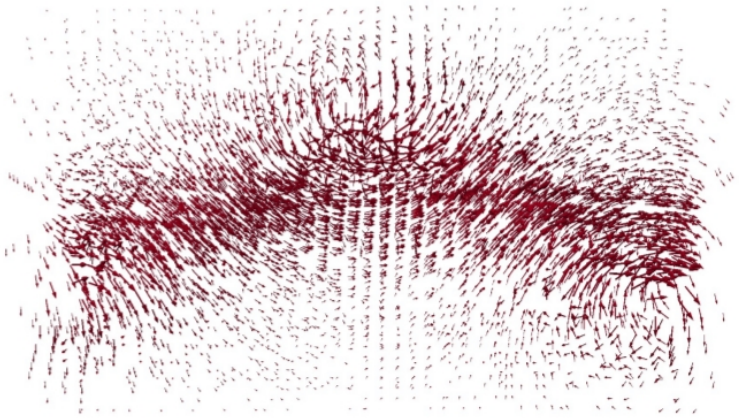

Figure 4.25: Side view of the external velocity field generated by a filament with an advance of six.

4.2.1 Further analysis with the numerical model

The numerical method is versatile and examples that are more closely related to the wake behind a wind turbine can be made. The first example is the study of the velocity field generated by three filaments, generated by conventional wind turbines with 3 blades, and the hub vortex is modeled as a set of 9 helical vortices of smaller diameter. Fig. 4.26 shows the helical vortices with an advance equal to one, which simulate the tip vortices generated by blades of the wind turbine, as well as the set of the yellow vortices simulates the hub vortex. This figure shows that the filaments have the same behavior as a single helical vortex with the same advance, ie the axial component is predominant. The filaments are compressed enough, and each of them are influenced by others. The whole set moves a solid, whith little or not rotation.

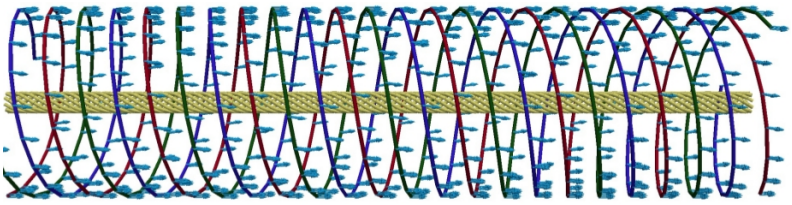

Figure 4.26: Side view of three filaments with an advance of one.

Fig. 4.27 shows a isometric view of the tip and the hub vortex, where we can see that all velocity vectors on the tip vortices are dominated by the axial component. The velocity vectors on the hub vortex are not shown, for clarity. The circulation that we have used for the hub vortex is one tehth of the tip votex, and has a little effect on the velocity field when the advance is equal to one. The lack of information on the velocities of hub vortex in the wake of a real wind turbine does difficult to choose an adequate magnitude for circulation, although it is known that their influence is minimal when the advance is small [38]. Also, we consider that the radius of the hub vortex is constant, which has been previously proposed in the literature [36].

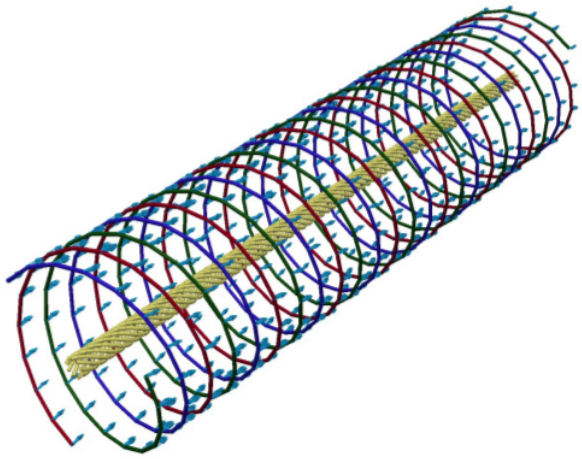

Figure 4.27: Isometric view of three filaments with an advance of one.

Fig. 4.28 shows a side view of the interior and exterior velocity field produced by the tip vortices and the hub vortex, where we can see that the field generated by three filaments are concentrated in the interior field, being predominantly in the axial direction just as it happened with the velocity field generated by a single filament. We can also see that practically there is not influence with the exterior field. The three filaments act as physical borders which keep the flow inside the vortex tube. But unlike the field obtained with a single filament, the velocity field for multiple filaments shows that in the boundary between the interior and exterior field there is not formation of recirculations.

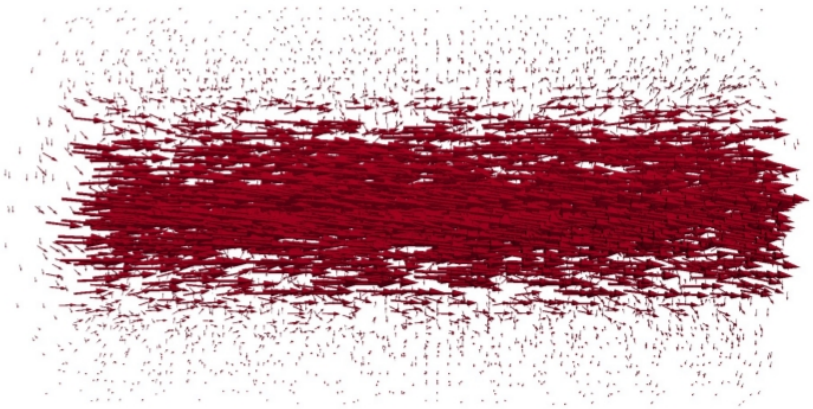

Figure 4.28: Side view of the interior and exterior velocity field generated by three filaments with an advance of one.

We consider now a system of three filaments as tip vortex, and the hub vortex, with an advance of $2\pi k = 6$ where the filaments are more expanded. Fig. 4.29 shows a side view

of the tip vortices and the hub vortex. The velocity vectors on the tip vortex tend to be tangent to the filament.

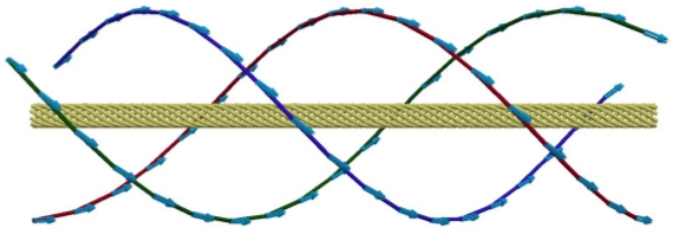

Figure 4.29: Side view of three filaments with an advance of six.

Fig. 4.30 shows a side view of the set of vortices, where we can see that velocity vectors of tip vortices seem to be tangential at all time to their rescpective filament, which it differs from the behavior shown by a single filament. This indicates that if there is an interaccion between them, which causes the vortices have the same behavior among them.

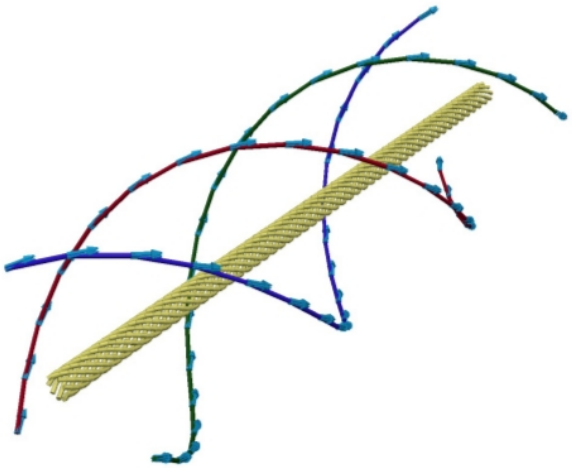

Figure 4.30: Isometric view of three filaments with an advance of six.

Fig. 4.31 shows a side view of the velocity field produced by the three filaments. For this advance, we see that there is an increase in the interaction with the exterior field. Further, it can be observed that in the exterior field the azimuthal component seems to predominate, whereas in the region contained by the three filaments appears that the axial component dominates. We can aslo note that there are certain vectors that describe the behavior of the filaments, these vectors can be seen over the axial region, as if they were those who contain it.

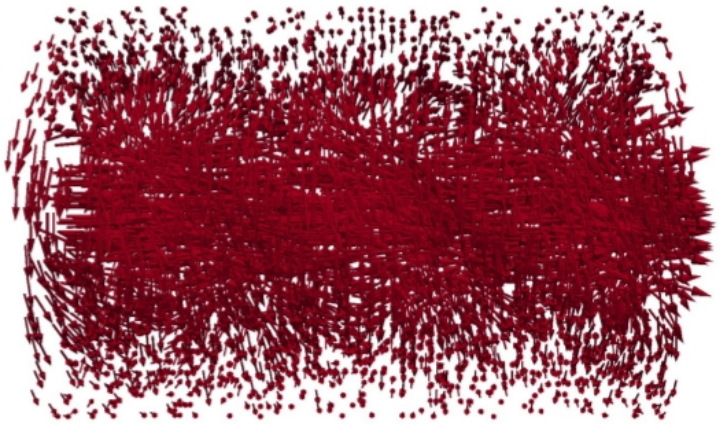

Figure 4.31: Side view of the interior and exterior velocity field generated by three filaments with an advance of six.

Fig. 4.32 shows a isometric view of the interior and exterior velocity field, where we can see that if there is an increase in the azimuthal component in the surroundings, as well as the existence of a central region where the vectors move preferentially in the axial component, approaching to the behavior shown by the filaments with an advance equal to one.

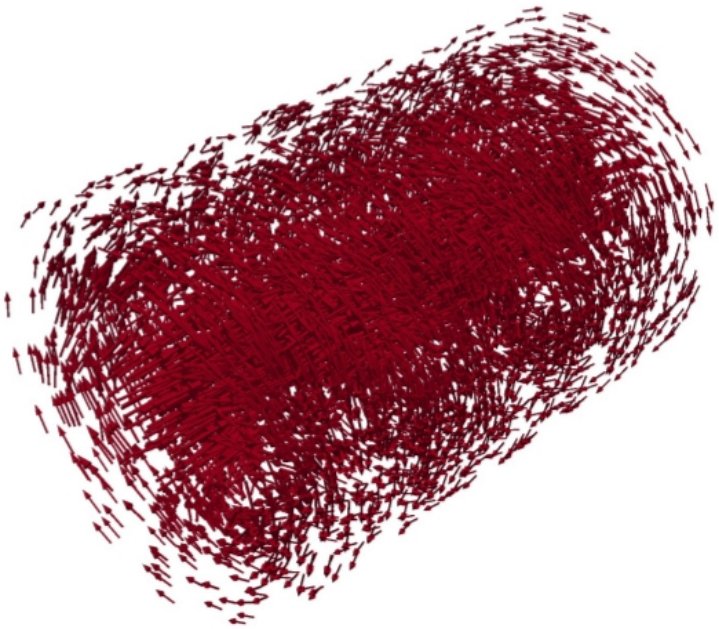

Figure 4.32: Isometric view of the interior and exterior velocity field generated by three filaments with an advance of six.

4.3 Study of consistency of the models

4.3.1 Convergence of the series in the analytical model

As it was briefly mentioned in previous sections, the results obtained with the two models differ in some cases. The difference is more marked in the axial component when the advance is equal to one. In order to identify the origin of the discrepancy we carried out and analysis of the convergence of the series and also in the number of points that compose the vortex filament.
We evaluated the analytical solution with 20, 40, 60, and 80 terms in the series and plotted the velocity distributions, and we found that starting from 20 terms the curves converge. Fig. 4.33 shows the axial component of the velocity field obtained with Hardin's model using 80 terms in the series. We see that the result obtained is indistinguishable from those calculated with 20 terms, despite increasing the number of terms in the series the graph does not change. We expected that increasing the number of terms in the series, the sudden growth of the component Uz did not happen.

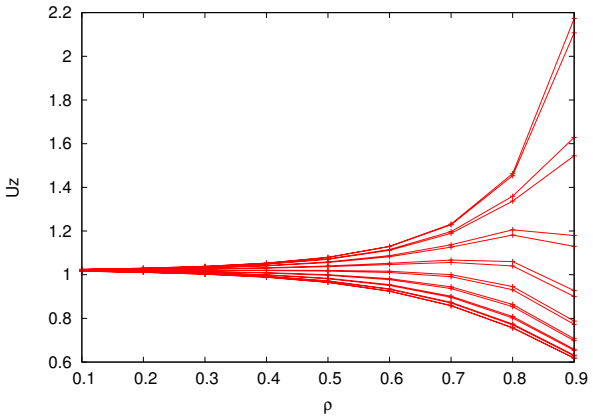

Figure 4.33: Component Uz of the analytical solution with 80 terms in the series.

To further explore the convergence of the analytical solution, we evaluate the series in two extreme cases, one with a very small advance, and other with a large advance. The results show that when the advance is equal to 0.003, the axial component is as expected for all values of Uz as a function of ρ, for all points except for the last one, ie. the one closest to the edge, where we again note that the series do not converge. This study showed that for all values of ϕ, the axial velocity is Uz is constant, and it does not depend on the angular or radial coordinate, this is because the filament is very tightly coiled. When the advance is equal to 300, the axial component presents the same behavior of when the advance is equal to one, and this is understandable because it is an infinite straight filament. The only variation are the magnitudes of the axial velocity, since being a more expanded filament there is a greater presence of the radial and azimuthal components.
Fig. 4.34 shows a study of the mesh of the velocity field generated by the analitical

solution. In this figure, we can see that for $\rho \leq 0.9$ the values of the axial component (Uz) do not vary regardless the number of nodes in ρ. This study was done for a number of nodes in ρ of 10, 100 and 1000. In order to observe the behavior of the axial component when $\phi = 1.745$ rad, because for this ϕ, Uz showed to become larger than other values of ϕ. In the figure, it can be seen that when the number of nodes is equal to 100 or 1000, the curve of Uz reaches values of up to 4.7, as ρ approaches a. But in addition, the curve of 1000 nodes shows that this reaches a maximum value and then decreases up to 3.3.

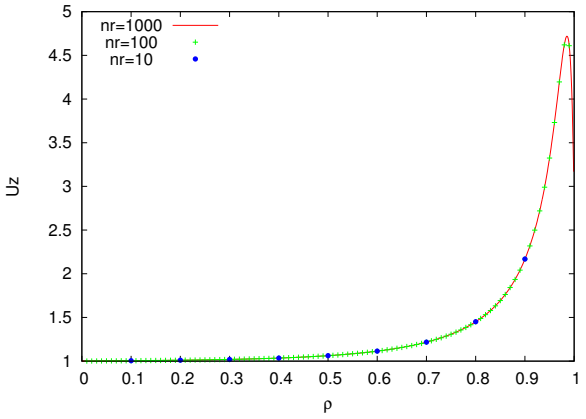

Figure 4.34: Axial component (Uz) of analitical model as a function of ρ, with $\phi = 1.745$ rad.

4.3.2 Number of nodes in the filament and mesh convergence in the numerical method

The analysis of the convergence of the results obtained with the numerical method as a function of the number of nodes in the filament was done to ensure convergence. Fig. 4.35 shows the axial component of numerical model, with 80 nodes in the filament. The graph shows that when we increase the number of nodes, the results do not change as compared with that obtained with 20 nodes (see Fig. 4.14). This study was done by numerically calculating the velocity field for a number of nodes equal to 20, 40, 60, 80. The results show that the behavior of the axial component is the same, regardless of the number of nodes. The study for a very small and very large advance was also done with the numerical method. The results indicate that when the advance is equal to 0.003, Uz has the same behavior shown in Fig. 4.35, ie the component has a greater value in the center, and as we move toward the edge, it decreases. But in addition, it was observed that for all values of ϕ, Uz has the same magnitude, ie equal to the analytical solution. As expected, the numerical solution is independent of the angular coordinate with an advance of 0.003, but the reduction of its magnitude of the velocity with respect to ρ is still not understood. The numerical and analytical methods match in many features, perhaps the discrepancy between the results is due the analytical model is based in an infinite helical vortex, in contrast the numerical model is based in a finite filament. Or

maybe we have not yet found which are the conditions to which the method approximates the Hardin's model. With an advance equal to 300, the model had the same behavior showed by the graph of an advance of six (see Fig. 4.21), with the only difference that the magnitudes of the component were lower, this is due to the expansion of the filament, which causes a gain in the angular velocity.

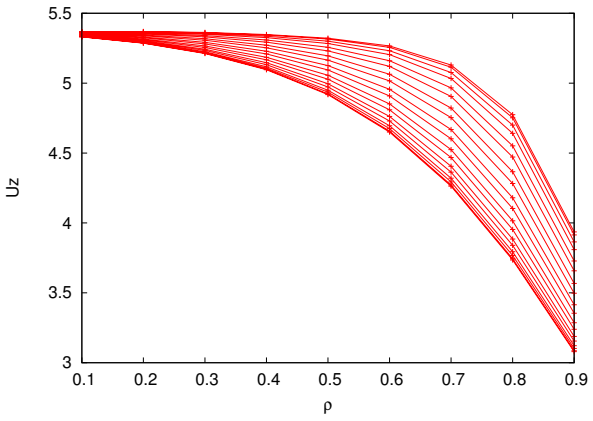

Figure 4.35: Axial component (Uz) of the numerical solution with 80 nodes in the filament.

It is worth mentioning that to rule out that the reported results are due to the lack of mesh refinement in the domain, we also did a study of the mesh, by using two and three times as many nodes. Fig. 4.36 shows the curves of the a single axial component for a mesh refinement in the nodes of ρ. The results did not have any change regardless the number of nodes in ρ, ϕ and z. This study was developed for the filament with 80 nodes.

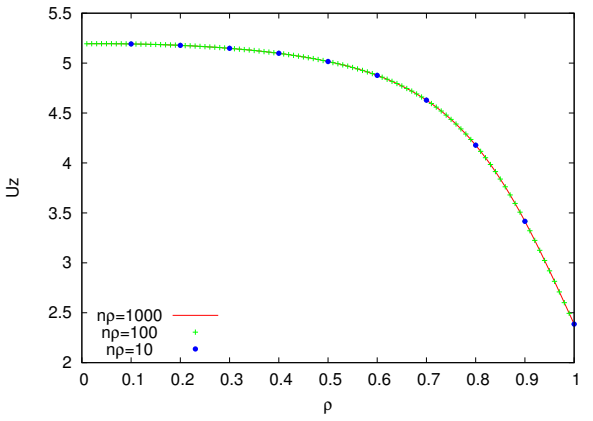

Figure 4.36: Axial component (Uz) of the numerical solution as a function of ρ, with $\phi = 6.282$ rad.

4.3.3 Finite vs infinite helical vortex

The infinite extension of the helical filament is an implicit assumption in the analitical model. In contrast, the filament in the numerical method is necessary finite. In order to justify the comparison of the results of the two different models, we made the following analysis. Fig. 4.37 shows the average velocity Uz as a function of z. In this graph we see that the numerical model shows edge effects in the first and the last 30% of domain, but between these range; there is a plateau. When the advance is less than or equal to 2, the model tends to form this distribution in its axial component. This region becomes larger as the filament gives more rotations. The development of this zone is important because it is where the numerical calculations are more appropriate, and the behavior of the filament is closer to the an ideal helical vortex. Fig. 4.35 was obtained from the central region of Fig. 4.37, and subsequent studies emphasized its importance in the determination of the Cp.

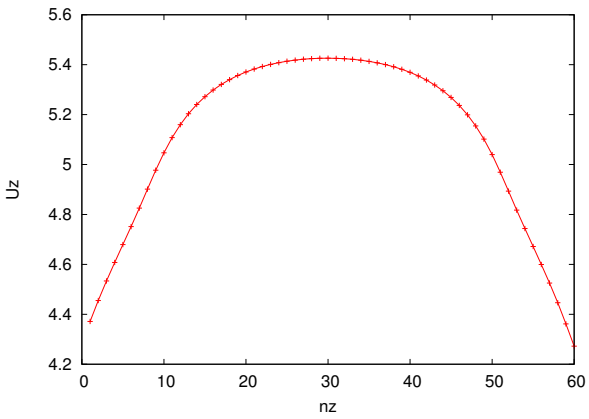

Figure 4.37: Average velocity Uz as a function of z.

4.4 BEM and Vortex Rankine

In the study of the BEM we use a model developed by Tavares and co-workers, which takes into account the geometry of the wake by using a Rankine vortex. The model was analyzed using the aerodynamics characteristics of the NACA 0012, and an angle of attack of 8°, as Tavares and et al. did. The main difference between their analysis and ours is the calculation of the Prandtl tip loss factor, since they calculated it according to Wilson [38], and we do it according to the Wind Energy Handbook [28].
To calibrate our results, we checked the behavior of the model to a tip speed ratio of 1.57. Fig. 4.38 shows the evolution of the theoretical power coefficient as a function of the number of iterations. We see that the model converges to a number of iterations larger than 18, which it differs with results obtained by Tavares, because in their simulations the model converges to a number of iteration larger than 25. We can also see that when $N = 0$ the model exceeds the Betz limit for a number of iterations less than 18, as it was reported by Tavares. But when $N = 1$ or 2, the model does not exceed Betz limit. This is another difference with the results reported by Tavares, in which their simulations exceeded Betz limit for these values of N, and for a number of iterations less than 25. Further, we can see that for $N = 1$ or $N = 2$, the value of Cp is less than the Betz limit (59.26%), and this is due to the Rankine vortex, according Tavares. As well as when $N = 0$ the Cp is 59.75%, which is slightly larger than the Betz limit, due to the fact that the free vortex asumption causes infinite velocities on the wake near the axis of the wind turbine.

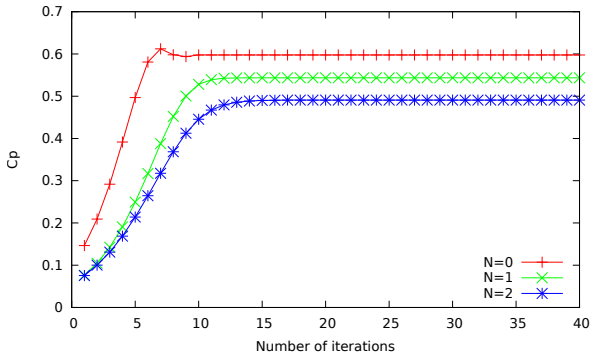

Figure 4.38: Power coefficient as a function of the iterations for $X = 1.57$.

Fig. 4.39 shows the behavior of the induction factors in the rotor plane and the wake, in which we can see that these converge to a number of iterations larger than 10. The convergence values for the induction factor are: $a = 0.3342$, $b = 0.7375$, $a' = 0.6175$, $b' = 1.3663$; they agree with those reported in reference [38].

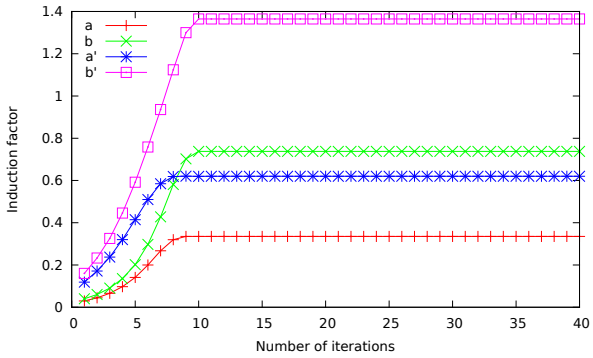

Figure 4.39: Induction factors in the rotor plane and in the wake for $X = 1.57$.

These results were obtained for a small wind turbine with multiple blades, typically used in pumping systems, with 3 m diameter and 0.9 m hub diameter, constant rotation of 60 rpm, average wind speed of 6 m/s, and 12 blades, giving a tip speed ratio of 1.57. Fig. 4.40 shows the chord distributions, in which we can see that the results differ from those presented by Tavares and co-workers, and this occurs in values of the chord lower of 0.4, then the values of the chord have a good agreement in the central zone up to the point 0.95, and at the end part the values again differ, although in this part the values are closer to the ones reported by Glauert and Stewart as reported by Tavares [38]. These differences may be due to the calculation of the prandtl tip loss factor, which one has a direct implication in the calculation of the chord.

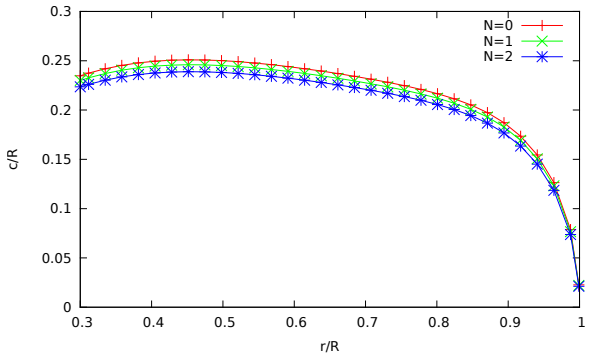

Figure 4.40: Chord distributions for $X = 1.57$.

Fig. 4.41 presents the twist angle distributions for the previous turbine. We see that the results agree entirely with those shown by Tavares. So we can say that the tip loss factor has only inference in the chord. The graph of Cp and the induction factor presented above, both have been obtained for this turbine, but Tavares does not specify the data of turbine (diameter of turbine and hub, average wind speed, etc.) that he used to obtain these graphs, so we could attribute the discrepancies to this.

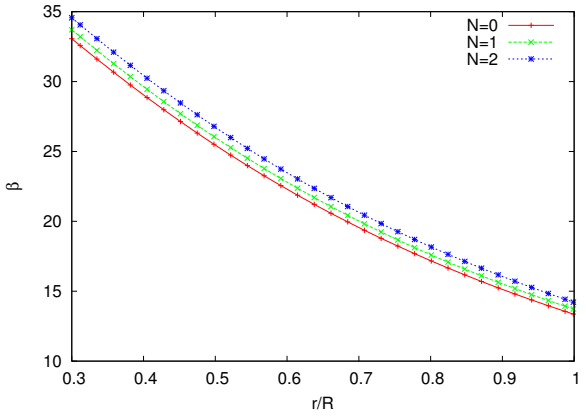

Figure 4.41: Twist angle distributions for $X = 1.57$.

In the second part of this section we discuss the results obtained from the model for $X > 2$, i.e. for high tip speed ratios. These results were obtained for $X = 4.18$, and for a small wind turbine with 4 m of diameter, 0.4 m of hub diameter, constant rotation of 120 rpm, average wind speed of 6 m/s and 3 blades. Fig. 4.42 shows that the power coefficient tends to the Betz limit regardless of the value of N. Further, we can see that the model converges for 15 or more iterations. Only the graph of $N = 0$ becomes larger of the Betz limit. All others display a monotonous convergence. In the results reported by Tavares, the model converges to a number of iterations larger of 20, and for all values of N, it takes values larger than the Betz limit when the iterations are lower of 20. But again, the discrepancies may be due to the lack of specification of the data of turbine to which Tavares obtained the graphs of Cp and induction factors.

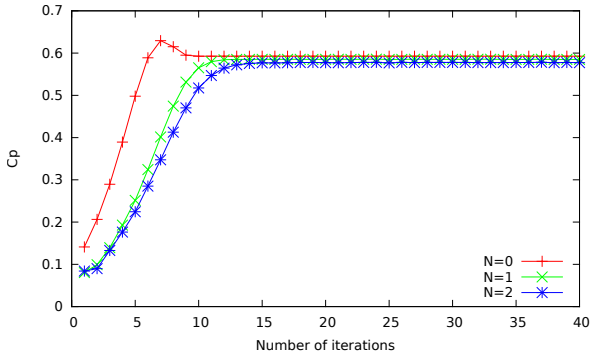

Figure 4.42: Power coefficient as a function of the iterations for $X = 4.18$.

Fig. 4.43 shows the behavior of the induction factors for $X = 4.18$, in which we see that they converge for a number of iterations larger of 10. Further, we note that the values of convergence are: $a = 0.3333$, $b = 0.6817$, $a' = 0.7325$, $b' = 1.4953$, the most of these

values not agree to those reported by Tavares and co-workers, in general all values are larger, excluding to a which coincides.

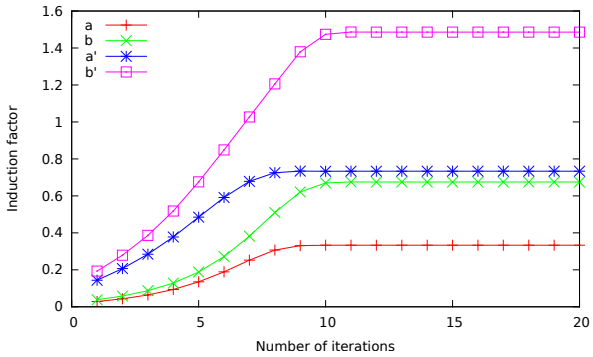

Figure 4.43: Induction factors in the rotor plane and in the wake for $X = 4.18$.

Fig. 4.44 shows the chord distributions. As can be apreciated, the chord is the same for different values of N. These values differ in the initial part to those presented by Tavares and co-workers, their results start at 0.09 and then the values grow rapidly to 0.3, showing that there is a discrepancy in the values of the chord near of the hub vortex. Moreover, our results start in 0.3, then the values grow slightly. For the range of 0.2 to 0.9, the results have a good agreement with those reported by Tavares. In contrast, in the range of 0.9 to 1 the values do not match with those reported by Tavares, but our results are closer to those shown by Stewart and Glauert. Also, it is worth mentioning that both Tavares and co-workers, as Stewart and Glauert, and our results have a good agreement in the central zone, and only at the extremes we can observe discrepancies between models.

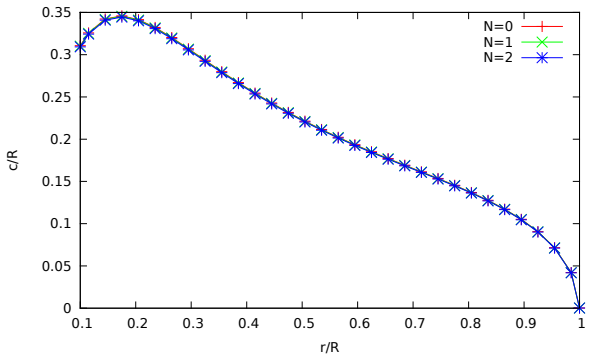

Figure 4.44: Chord distributions for $X = 4.18$.

Fig. 4.45 shows the twist angle distributions. All the three graphs show the same behavior, as well as a good qualitative agreement. Our results agree entirely with those reported by Tavares.

In the graphs presented above there are discrepancies in the of Cp and the induction factors for both cases of study (high and slow tip speed ratio). As mentioned above these discrepancies may be due to different input data from those used by Tavares and co-workers. We were forced to proceed this way since they do not report the whole set of data used to obtain the graphs. In the graphs of chord and twist angle, where the data of our study and Tavares are the same. The results obtained shows that there are discrepancies with the reported only in the extremes of the chord graphs. This may be due to tip loss factor used, since we used a different one to the reported, because we could not get the reference in which Tavares and co-workers based their study. Further, it appears that the twist angle is not affected by the choice of the tip loss factor, since the distributions graphs did not present variations with the reported, for different values of X.

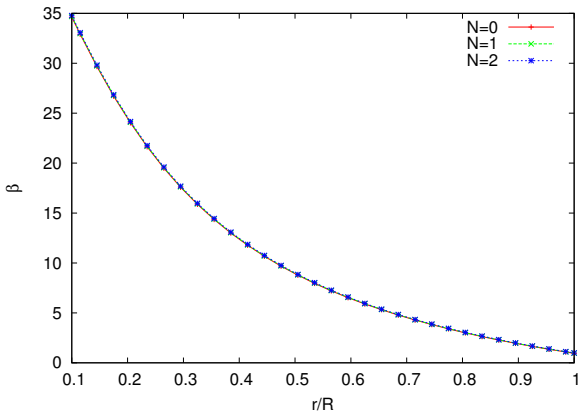

Figure 4.45: Twist angle distributions for $X = 4.18$.

4.5 Incorporation of the wake model

In this section the helical vortices are used for describing the wake, and from them the velocities are obtained to be connected to the model of Tavares and co-workers. These velocities are the averages of the axial and azimuthal velocity obtained from a cross section of the velocity field located in the far wake. The graphs presented below were obtained with the same conditions of those of the Rankine vortex.
Fig 4.46 shows the power coefficient obtained from the helical wake for $X = 1.57$, which it is compared with the results of the Rankine vortex. We can see that in the first iterations, the helical wake model presents a wide variation in the first 10 iterations. For a number of iterations larger than 15, the model converges, and coincides with the results obtained of Rankine vortex with $N = 0$. The Cp obtained with the helical wake model converges to 59.99. Also, we can see the helical wake model marginally exceeds the Betz limit as Rankine vortex does for $N = 0$, which, according to the actuator disk theory is not possible.

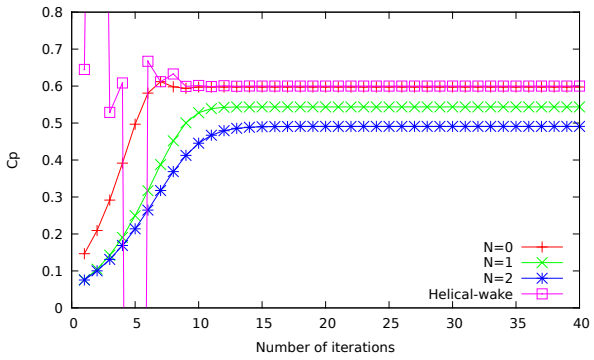

Figure 4.46: Power coefficient as a function of the number of iterations, for $X = 1.57$.

Fig. 4.47 shows the induction factors as functions of iterations. We see that all of them take 10 iterations to converge except b', which it has very small values all along. The values of convergence are: $a = 0.2238$, $b = 0.3398$, $a' = 0.4874$, $b' = 1.2351E - 09$. Fig. 4.48 shows the chord distributions obtained from the helical wake. From this graph we find that the aerodynamic shape is far from that presented by the Rankine vortex. This figure shows that in contrast to the results presented by the Rankine vortex, the graph of the helical wake does not present an ascending it, and from the beginning (0.171) has a negative slope, only in the last values ($2.2682311E - 02$) it has a similar behavior.

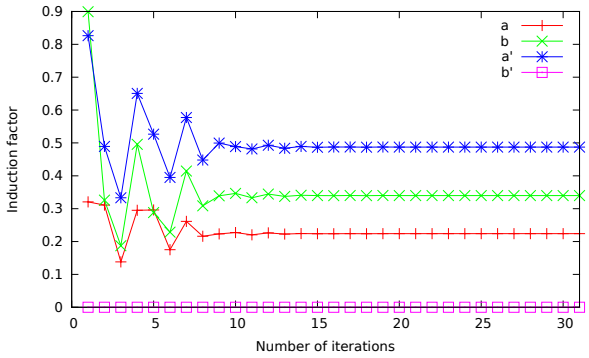

Figure 4.47: Induction factor of the helical wake, for $X = 1.57$.

Fig. 4.49 shows the twist angle distributions obtained from the helical vortices. We see that the graph has the same qualitative behavior of the graphs of the Rankine vortex. But, the results suggest a systematic increase in the angle of attack, as compared with the Rankine vortex model.

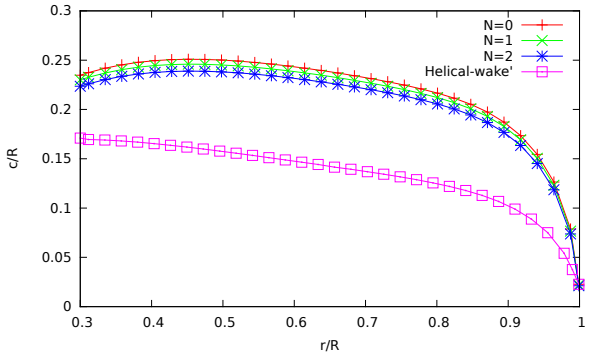

Figure 4.48: Chord distributions for $X = 1.57$ as a function of r/R.

The graphs presented above of the helical wake were obtained of the equations of the Rankine vortex for $N = 0$, when we used the values of $N = 1$ or equal to 2, the graphs of Cp exceeded the Betz limit by far (~ 0.7), tended to values of 0.7, which is not possible, so we decided not to use these values of N with the wake model. For this particular case, where $X = 1.57$ and the turbine has 12 blades, the model presented difficulties to converge. Due to the presence of 12 helical vortices, the wake is very intense and the average velocities are very large. To overcome this difficulty we had to change the circulation of the helical vortices, until the model of Rankine vortex converged using the average velocities calculated in the wake.

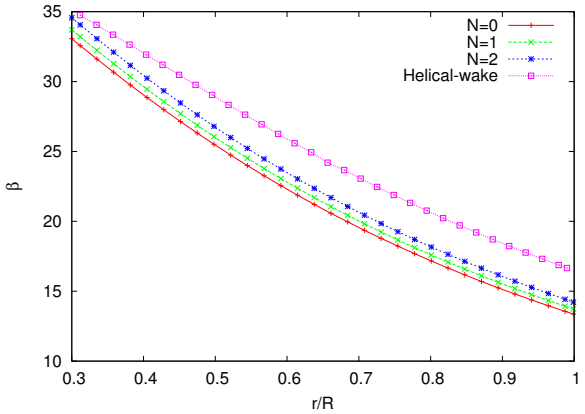

Figure 4.49: Twist angle distributions for $X = 1.57$.

Now we discuss the behavior of the helical wake for high tip speed ratios, ie for $X = 4.18$. Fig. 4.50 shows the power coefficient as a function of the number of iterations, and this is compared with the results of the Rankine vortex with the same conditions. We see that the wake model for a number of iterations less than 10 exceeds the Betz limit, and for a number of iterations larger than 20, it converges. But a detailled look indicates an oscillating damped. After 40 iterations the Cp is 59.18, which is a slightly lower than 59.26 presented by the Rankine vortex with $N = 0$.

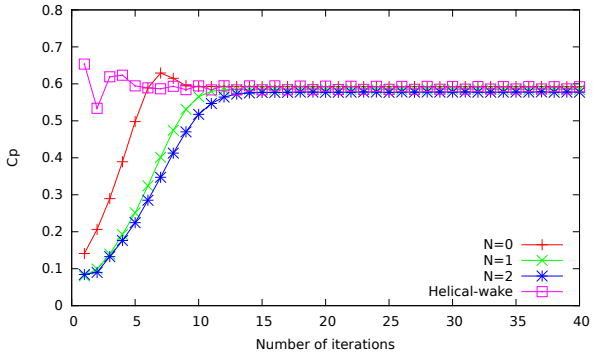

Figure 4.50: Power coefficient as a function of the number of iterations, for $X = 4.18$.

A more exhastive analysis of convergence (see Fig. 4.51) indicates that after 100 iterations the Cp converges to 58.97 with variations smaller than in the previous figure.

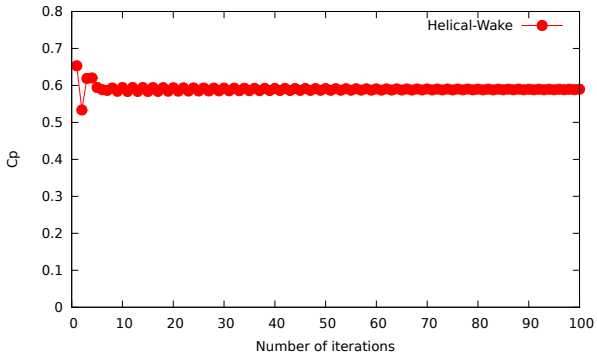

Figure 4.51: Power coefficient of the helical wake as a function of the number of iterations, for $X = 4.18$.

Fig. 4.52 presents the induction factors for $X = 4.18$, and 100 iterations. At the beginning of the iteration procedure the model has certain dispersion (iterations < 40), the model converges for 70 iterations. In the final region we can see as a plateau is formed, where we can observe how the model converges. The trend previously described applies for a, b and a', but not for b', which from the beginning does not vary, and have values that tend to zero. The values of convergence for the induction factors are: $a = 0.1902$, $b = 0.2731$, $a' = 0.4567$ and $b' = -3.7422E - 05$.

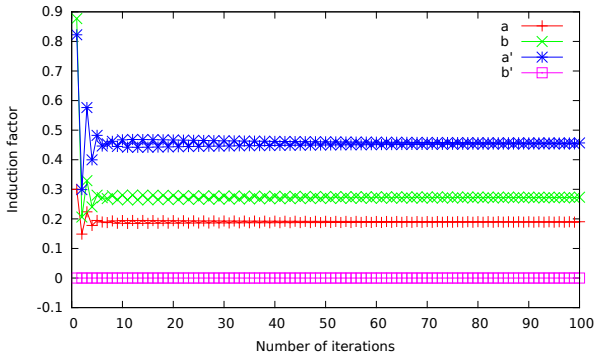

Figure 4.52: Induction factor of the helical wake,for $X = 4.18$.

Fig. 4.53 shows the chord distributions obtained from the helical wake. The results differ from those obtained for the Rankine vortex. For values smaller than 0.3 of the horizontal axis (r/R), we see that the Rankine vortex shows an increase in the chord, in contrast the helical wake where the chord decreases from the starting value. For values larger than 0.3, it can be seen that there is a qualitative concordance between the models.

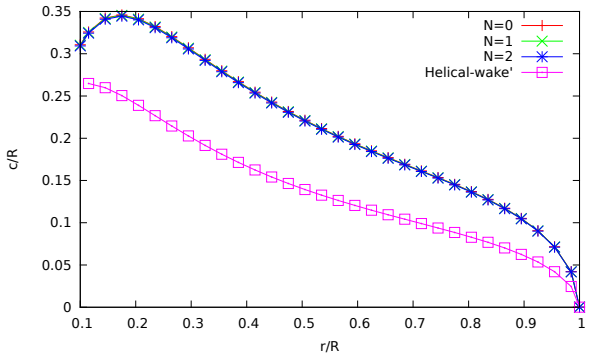

Figure 4.53: Chord distributions of the helical wake, for $X = 4.18$.

Fig. 4.54 shows the twist angle distributions obtained from the helical wake. The results show a good qualitative agreement with the Rankine model. Further, this results suggest a slight increase in the angle of attack.
The results for $X = 4.18$ were obtained with the same conditions of the Rankine vortex with $N = 0$, For this study the helical wake converged faster than the previous study, this was due to that this time the turbine of study only has 3 blades, which it does not generate an intense velocity field, therefore the average velocities are not large, and can be adjusted more easily to the BEM theory. It is worth mentioning that although this time the wake was only represented by three helical vortices, it was necessary to adjust the value of the circulation to ensure the convergence of the model.

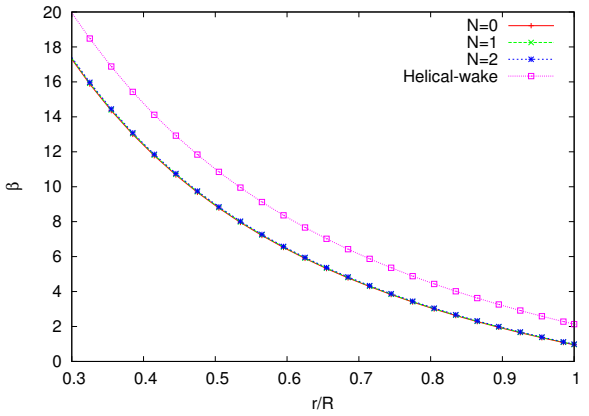

Figure 4.54: Twist angle distributions of the helical wake, for $X = 4.18$.

The results of this section show that when we combine the helical wake with the BEM, it is necessary to take into account the circulation, because this coupling between the two models is done using the calculated velocities in the wake. Wood mentioned this dependence, and he concluded that when the BEM is used with some type of wake model

is necessary to take into account the circulation from the forces acting on the blade. When $X = 4.18$ the induction factor b' tends to negative values, and it is because with this tip speed ratio appears negative angular velocities in the wake. This had already been observed by Wood, and he attributed to the fact for a high tip speed ratio , the wake can have a significant expansion, causing negative speeds, although he defined a high tip speed ratio as $X > 8$.

		Rankine vortex		Helical wake
X	N=0	N=1	N=2	N=0
1.57	59.75	54.35	49.08	59.99
4.18	58.48	57.73	57.73	58.97

Tabla 4.1: Power coefficient obtained of the different turbines studied.

Table 4.1 shows the Cp obtained from the different models, where we can see that the results showed by the helical wake are not far away from the Rankine vortex, mainly with $N = 0$. The results are better than expected, since the equations used in this study were developed for a wake with a Rankine vortex geometry, and not for a wake with a helical geometry, which takes into account the average velocity in it. In addition , the study showed that when N is greater than 0, the helical wake exceeds the Betz limit, both for a high and low tip speed ratios. This is because the parameter N represents the influence of the Rankine vortex. One of the limitations of the model is the determination of the circulation. A more robust model would be to implement its calculation in the iterative process, as it was done by Wood in [34, 35].

Chapter 5

Conclusions

5.1 Conclusions

The analytical model described in Section two exhibits a good general qualitative agreement with the results expected for a helical vortex with an advance equal to one. However, it is important to remark that the series solution have slow convergence (on even divergence) in some specific cases. This problem is specially acute in the axial velocity, when it is calculated near the position $r = 1$. These uncertain results manifest themselves clearly in the graphs of the velocity field, where we see how the vectors that are closest to the edge are larger than expected, and have a major interaction with the exterior velocity field. These results suggest that we should have some caution when using the analytical solution of Hardin, since apparently the lack of convergence occurs not only on the edge as Hardin himself points out, but it is also observed for some values of the axial component for some values of ϕ. The results for an advance equal to six were obtained with the idea of analyzing the behavior of the analytical model to an advance greater to one. We observed that for this advance, the vorticity is concentrated in the filament, and only the vectors that are nearest to the it are affected by its presence. The graphs show that to this advance there is an increase of the angular velocity in the velocity field, which coincides with the reported in the literature. We can conclude that the model behaves qualitatively as expected to the different advances, but the lack of data reported in the literature makes it difficult the analysis, since most studies focus on the filament dynamics and not the velocity field.

The numerical analysis shows that when the advance is equal to one, the radial and azimuthal velocities have a good qualitative agreement with the analytical model in some regions, especially the radial component. The axial component shows larger differences, since it is more intense at the origin and it decreases toward the edge. This was observed for all values of the axial velocity as ϕ varies. This contrasts with the results of the analytical model in which some values of the axial component of the velocity decrease and others increase. The velocity field obtained from the numerical model shows that the field is completely dominated by the axial component with this advance. Further, it was observed that both the numerical and analytical model showed the formation of the same number of localized vorticity at the edge, which are due to the presence of the filament. Moreover, the results of the numerical model are closer than expected to those found in the literature, since the graphs of the field show that the velocity is confined within the interior field. The results for an advance equal to six showed that the numerical method

has a good agreement with the qualitative behavior of the analytical model. Further, the models had quantitative agreement in some regions. From the results of the numerical model with three filaments, it was observed that the wake becomes more intense, and when the advance is equal to one, the flow is confined to the tube of vorticity bounded by the filaments, which is consistent with the behavior that the wake must have according to the literature for studies of turbines with two or three blades. The results for three filaments with an advance equal to six showed that the angular momentum growing in the field, also there is a greater interaction with the exterior field and the flow is not confined. The study of an advance or a suitable pitch in the design of a wind turbine is an issue that is still under investigation, as this has a direct impact on the energy that can be extracted from the wind, as well as we have observed may have relation to the mechanical stresses to which the turbines are subjected, from these turbines could be in its same or in the wake of another turbine. In the literature has reported that the turbines fail in less time that it has been estimated, according to its design, so that the choice of a suitable pitch is very important, such that the trail of vortices is enough far away from turbine, but so that it can be dissipated before reaching a second turbine. Conclude that the model presentes a good agreement with the velocity field reported in the literature. The lack of experimental studies on the velocity field in the wake of a wind turbine makes it difficult to validate the model, especially for an advance equal to six, and only proceed based on assumptions.

To study of convergence we focus on the axial component because of this we know that when the advance is equal to one, the behavior of the component practically does not vary in the radial or angular directions. The results showed that indeed the Hardin model has a certain degree of non-convergence for some values of the axial velocity, as ϕ varies. Further, it was showed that the numerical model does not behave in all cases as does the analytical model, but nevertheless the two models have coincidences. The numerical model did not show to be influenced by the number of nodes in the filament or in the domain. So we can conclude that the lack of coincidence of the numerical model with the analytical model for an advance equal to one may be due to the fact that the numerical calculation is based on in finite filament, and the analytical model assumes that the filament is infinite. Moreover, the behavior that we know ($Uw = cte$ for any value of r and ϕ) that is expected for $2\pi k = 1$ is for an ideal and infinite helical vortex, for what the behavior of the numerical method is not necessarily wrong.

The study of the Rankine vortex model showed that for a low tip speed ratio the results coincide with the reported by Tavares and et al. The main differences were found in the graphs of Cp, and chord. The values of Cp agreed with those reported, but also exhibited a slight change in their behavior when $N = 1$ or 2. The results for Cp did not exceed the Betz limit at any time, as well as all graphs of Cp converged faster than those presented by Tavares. The chord calculated in the present work has differences in the initial values, which were larger than those reported by Tavares et al. The twist angle distribution coincides both qualitatively and quantitatively with Tavares. We conclude that the analysis of the model agrees with that reported by Tavares and that the discrepanciesa are likely to be due to the incomplete set of parameters and initial values reported by Tavares. We also conclude that the chord is strongly influenced by the tip loss factor, mostly near

of the hub vortex. The results of the Rankine model for a high tip speed ratio show that there is certain coincidence with the results reported by Tavares. The graphs of Cp showed to converge to the same value reported by Tavares, we observed discrepancies in the behavior of power coefficient when N is equal to 1 and 2. The induction factors have a good qualitative agreement with the reported, but not quantitative. Further, the graph of chord distribution showed again that the initial values does not match with Tavares, but the twist angle distribution presented to have a good agreement both quantitative and qualitatively with those reported by the cited authors. Our overall conclusion is that our analysis has a good qualitative concordance with Tavares, and that the discrepancies in the chord are due to the different tip loss factor, since this variable has a strong incidence in its calculation. Further, that the lack of specification of input data makes it difficult to analize the graphs of Cp and induction factors. In general, we also conclude that further study is needed of the interaction of the tip loss factor with the chord, since not only our results do not match with of the Tavares, their results also does not agree with Stewart and Glauert's, and the major differences between all models are noted near of the hub vortex and tip of the blade.

The study of coupling of the helical wake to the blade element theory through the Tavares model showed that for a low tip speed ratio, the convergence is reached, although this model was not developed for a helical geometry, and this is noted mainly when the factor N has values of 1 or 2. The graph of Cp had an unstable behavior for the initial values of Cp, until this becomes stable and reaches the convergence. This same behavior is observed for the induction factors. The value of Cp exceeded the Betz limit and it was slightly greater than to the obtained with the Rankine vortex with $N = 0$. The graph of chord distribution presented a qualitative change with respect to the Rankine model, besides the values of chord were smaller than all values obtained of the Rankine vortex for different N. The graph of twist angle had the same behavior of the Rankine vortex, but with a consistent overestimation. Further, the results were heavily influenced by the circulation. The general conclusion of this part is that the helical wake yields ood results for a wake model that is not developed for a helical geometry. The decrease in the chord and increase in the twist angle must be more deeply investigated, since in these results is noted the presence of the helical vortex, and their inclusion in the determination of the aerodinamic shape, which can be important, as it has been reported by previous authors. Other important conclusion is that the coupling between the BEM theory and the helical wake is strongly influenced by the circulation. In our model we observed that this parameter determines the convergence of the model; this effect has also be observed in the literature [34, 35]. The results of coupling for a high tip speed ratio showed that the helical model took more iterations to reach the convergence for Cp, but when it did, this did not exceeded the Betz limit. The induction factors had a similar behavior, but also it was noted that the factor related with the angular velocity in the wake had values that tend to zero, and sometimes to negative values, which coincides with the literature [36]. The graph of the chord suggests again that this variable must decrease. The twist angle distribution returned to show an increase in their values. This has a good qualitative agreement with the reported by Tavares, and it is very near to the Rankine model. It was also observed that for this high tip speed ratio the angular velocity in the wake tend to

zero. We conclude of this section that the helical model yields an acceptable prediction of the Cp, since this has a close value to the Betz limit, which is good, since this model takes into account the geometry of the wake and the induced velocities in the wake. Further, is shows an improvement over the Rankine model results when N is equal to 1 and 2. We also conclude that the chord and twist angle must be investigated further, because these present a different aerodinamic shape, which could improve the performance of the wind turbine, since this model considers other factors that the Rankine vortex does not incorporate. From this study, we conclude that the helical wake presents good results for both tip speed ratio, but specially for high tip speed ratios, for which the model does not exceeds the Betz limit. An important conclusion is that the circulation has a strongly inference in the convergence of the model both a tip speed ratio high and a low. The model has a large possibility to study different prototypes of turbines, and that it can be improved if we consider another factors, which would make the model more realistic, and with better results.

5.2 Future work

As part of the conclusions, we suggest some topics of study that can improve the helical wake model and which we consider that must be taken into account in future works. These are:

- The vortex expansion.
- The developepment of a theory for the determination of Cp that is based in a helical geometry.
- A dissipation model.
- A study of instabilities.
- Comparison of the numerical method with the closed solution for monolopes and dipoles of Okulov [17].

Bibliography

[1] Y. A. Pykh I.G. Malkina. *Sustainable energy: resources, technology and planning.* Witpress, first edition, 2002.

[2] J. J. Kraushaar R. A. Ristinen. *Energy and the environment.* Wiley, first edition, 1999.

[3] A. L. Rogers J. F. Manwell, J. G. McGowan. *Wind energy explained.* Wiley, first edition, 2008.

[4] J. Twele R. Gasch. *Wind power plants.* Solarpraxis AG, first edition, 2002.

[5] Hansen O. L. Martin. *Aerodynamics of wind turbines.* Earthscan, second edition, 2008.

[6] F. R. Eldridge. *Wind machines.* VNR, second edition, 1980.

[7] Okulov V. L. Sø rensen J. N., Naumov I. V. Multiple helical modes of vortex breakdown. *Journal of Fluid Mechanics*, 683:430–441, 2011.

[8] Jay C. Hardin. The velocity field induced by a helical vortex filament. *Physics of Fluids*, 25(11):1949, 1982.

[9] V. L. Okulov. On the stability of multiple helical vortices. *Journal of Fluid Mechanics*, 521:319–342, December 2004.

[10] J. N. Sø rensen. Instability of helical tip vortices in rotor wakes. *Journal of Fluid Mechanics*, 682:1–4, August 2011.

[11] V. L. Okulov and J. N. Sø rensen. Stability of helical tip vortices in a rotor far wake. *Journal of Fluid Mechanics*, 576:1, March 2007.

[12] V. L. Okulov and J. N. Sø rensen. Instability of a vortex wake behind wind turbines. *Doklady Physics*, 49(12):772–777, December 2004.

[13] Levy H. and Forsdyke A. G. The steady motion and stability of a helical vortex. *Proc. R. Soc. Lond.*, 120:670–690, 1928.

[14] Sheila E. Widnall. The stability of a helical vortex filament. *Journal of Fluid Mechanics*, 54(04):641, March 1972.

[15] Betchov R. On the curvature and torsion of an isolated vortex filament. *Journal of Fluid Mechanics*, 22:471–479, 1965.

[16] Adebiyi A. On the existence of steady helical vortex tubes of small cross section. *Quarterly Journal of Mechanics and Applied Mathematics*, 34:153–177, 1981.

[17] Y. Fukumoto and V. L. Okulov. The velocity field induced by a helical vortex tube. *Physics of Fluids*, 17(10):107101, 2005.

[18] Gupta B. P. and Loewy R. G. Theoretical analysis of the aerodynamic stability of multiple interdigitated helical vortices. *AIAA Journal*, 12:1381–1387, October 1974.

[19] Leishman J. G. Bhagwat M. J. On the aerodynamic stability of helicopter rotor wakes. *American Helicopter Society*, 56:100–120, 2000.

[20] S ø rensen J. N. and Shen W. Z. Numerical Modeling of Wind Turbine Wakes. *Journal of Fluids Engineering*, 124(2):393, 2002.

[21] V. L. Okulov and J. N. Sø rensen. Maximum efficiency of wind turbine rotors using Joukowsky and Betz approaches. *Journal of Fluid Mechanics*, 649:497, April 2010.

[22] Sørensen J. N. Henningson D. Ivanell S., Mikkelsen R. Stability analysis of the tip vortices of a wind turbine. *Wind energy*, 13:705–715, 2010.

[23] Di Felice F. Felli M., Camussi R. Mechanisms of evolution of the propeller wake in the transition and far fields. *Fluids Mechanics*, 682:5–53, 2011.

[24] L.J. Vermeer, J.N. Sø rensen, and A. Crespo. Wind turbine wake aerodynamics. *Progress in Aerospace Sciences*, 39(6-7):467–510, August 2003.

[25] Leonard A. *Ann. Rev. Fluid Mech.*

[26] H. Lamb. *Hydrodynamics*. Dover, sixth edition, 1945.

[27] G. N. Watson. *Theory of bessel functions*. Cambridge University, second edition, 1944.

[28] T. Burton. *Wind energy handbook*. Wiley, 2001.

[29] Jens Nørkæ r Sø rensen. Aerodynamic Aspects of Wind Energy Conversion. *Annual Review of Fluid Mechanics*, 43(1):427–448, January 2011.

[30] van Kuik G. Sø rensen J. N. General momentum theory for wind turbines at low tip speed ratios. *Wind energy*, 14:821–839, 2011.

[31] Glauert H. Airplane propellers, in aerodynamic theory. *Springer*, 4:191–269, 1935.

[32] Walker S. Wilson R., Lissaman P. Aerodynamic performance of wind turbines. Technical Report ERDA/NSF/04014-76/1, Dep. Energy Washington, DC, 1976.

[33] V. L. Okulov and J. N. Sø rensen. An ideal wind turbine with a finite number of blades. *Doklady Physics*, 53(6):337–342, July 2008.

[34] Wood D. H. and Koh S. G. Formulation of a vortex wake model for horizontal-axis wind turbines. *Wind Engineering*, 15:196–210, 1991.

[35] Wood D. H. and Koh S. G. Implementation of a vortex wake model for horizontal-axis wind turbines. *Wind Engineering*, 15:262–274, 1991.

[36] Wood D. H. On wake modelling at high tip speed ratios. *Wind Engineering*, 16:291–303, 1992.

[37] Wood D. H. Including swirl in the actuator disk analysis of wind turbines. *Wind Engineering*, 31:317–323, 2007.

[38] Amarante A. L. Tavares J. Pinho A. C. Tavares D. A., Pinheiro J. R. Optimum aerodynamic design for wind turbine blade with a rankine vortex wake. *Renewable energy*, 55:296–304, 2013.

[39] Lissaman P. Wilson R. E. Applied aerodynamics of wind power machines. Technical Report NSF-RA-N-74-113, Oregon State University, 1974.

[40] Mesquita A. and Alves A. An improved approach for performance prediction of hawt using the strip theory. *Wind Engineering*, 24:417–430, 2000.